Porphyroclasts: Source and Sink of Major and Trace Elements During Deformation-Induced Metasomatism (Finero, Ivrea-Verbano Zone, Italy)

Stefania Corvò, Antonio Langone, Jose Alberto Padron-Navarta, Andrea Tommasi, Alberto Zanetti

geosciences

MDPI

Article

Porphyroclasts: Source and Sink of Major and Trace Elements During Deformation-Induced Metasomatism (Finero, Ivrea-Verbano Zone, Italy)

Stefania Corvò [1,2,*], Antonio Langone [2,*], José Alberto Padrón-Navarta [3], Andrea Tommasi [3] and Alberto Zanetti [2,*]

1 Department of Earth and Environmental Sciences, University of Pavia, 27100 Pavia, Italy
2 Institute of Geosciences and Earth Resources, National Research Council (C.N.R), 27100 Pavia, Italy
3 Géosciences Montpellier, Univ. Montpellier & CNRS, 34090 Montpellier, France; padron@gm.univ-montp2.fr (J.A.P.-N.); andrea.tommasi@gm.univ-montp2.fr (A.T.)
* Correspondence: stefania.corvo01@universitadipavia.it (S.C.); langone@crystal.unipv.it (A.L.); zanetti@crystal.unipv.it (A.Z.)

Received: 13 March 2020; Accepted: 18 May 2020; Published: 21 May 2020

Abstract: Petrographic and geochemical data for mylonites from a metric-scale shear zone in mantle peridotites from the Finero massif (Southern Alps) record large mineralogical and geochemical modifications compared to surrounding coarse-grained ultramafic rocks, which were pervasively deformed in presence of hydrous melts. The mylonites are composed by olivine and orthopyroxene and, less frequently, clinopyroxene, phlogopite, and pargasite porphyroclasts enclosed in a fine-grained matrix of phlogopite and olivine, with subordinate amounts of orthopyroxene, clinopyroxene, pargasite, and chromite. P-T estimates indicate that deformation occurred under granulite- to upper-amphibolite facies conditions. Field relationships and U-Pb dating indicate that the shear zone was active during Lower Jurassic and/or later, in an extensional setting at the western margin of the Adria plate, which led to the opening of the Alpine Tethys. The major and trace element composition of the porphyroclasts in the mylonites significantly differ from those in the hosting coarse-grained ultramafics. Porphyroclasts were chemically active during deformation acting as source (diffusion-out) or sink (diffusion-in) for some trace elements. The chemical modifications were promoted by the interaction with aqueous fluids and the composition varied from mantle- (enriched in Ni, Co, Li, Na, REE, Y, and Sr) to crustal-derived (enriched in Zn, K, Al, Ti, and Fe).

Keywords: mantle peridotite; shear zone; major and trace elements; mylonite; porphyroclasts; Ivrea-Verbano Zone

1. Introduction

Shear zone evolution is commonly associated to bulk and mineral chemistry changes due to fluid–rock interaction [1–3], since shear zones provide important conduits for fluid movement through the crust [4] and lithospheric mantle [5,6]. Fluid focusing and high time-integrated fluid–rock ratios in shear zones allow mass transfer processes that can strongly modify the chemistry of deforming rocks. The P-T conditions and the chemical potential for certain components imposed by the external aqueous fluid dictate the mineral reactions and the stability of synkinematic mineral assemblages, controlling the balance between enrichment/depletion of major elements [7]. Moreover, deformation processes can locally accelerate chemical diffusion, promoting chemical heterogeneity and fractionation of trace elements [8,9].

The element behavior during deformation has mostly been the subject of research based on bulk chemistry and major-element mineral compositions [1,3–6,10–15]. These investigations point

to enhanced mobility at the bulk rock and mineral (major elements) scale. Trace-element mineral compositions are also modified by fluid–rock interactions, but the extent of modification and the relative roles of the nature of the fluids and of the deformation are poorly constrained. Available data suggest that trace element fractionation (i.e., REE and Y), in particular between clinopyroxene and amphibole, can be strongly affected by the stability of fine-grained accessory minerals precipitated in trace amounts from aqueous fluids percolating shear zones, independently on the deformation style (brittle vs. ductile) and/or to the alteration degree of mineral assemblages [3,13].

This work focuses on the evolution of major and trace element compositions in protomylonites and ultramylonites developed in a metric-scale shear zone crosscutting mantle peridotites from the Finero Phlogopite Peridotite unit (Ivrea-Verbano Zone). This shear zone has been the subject of previous microtextural and geochemical studies [1,2,14–16], which demonstrated that bulk compositions (major and trace elements) and mineral chemistry (major elements) underwent significant changes during shear deformation. Here, major and trace element composition of porphyroclasts in protomylonites and ultramylonites, as well as the major element composition of matrix-forming minerals are compared to the mineral compositions in the surrounding coarse-grained ultramafic rocks. Field evidence and zircon dating allowed us to constrain the timing of the shear zone activity and to address the mineralogical and geochemical changes in the frame of the geodynamic evolution of the northernmost part of the Ivrea-Verbano Zone.

2. Geological Setting

The Ivrea-Verbano Zone (IVZ) occupies the westernmost part of the Southern Alps. It consists of a lower continental crust sliver of the Adria plate, which escaped Alpine subduction, interleaved with remnants of the lithospheric mantle at different crustal levels [17–19]. Among these mantle remnants, the most important are the Finero, Balmuccia, and Baldissero peridotite massifs, which outcrop within the lowermost units of the crustal section close to the Insubric line [20].

The mantle peridotites of Finero (Figure 1a) have been thoroughly investigated due to their peculiar features: they consist of fully-metasomatized mantle rocks characterized by pervasive crystallization of significant amounts of pargasite and phlogopite, which may locally attain up to 25 vol.% [16]. The mantle rocks (also referred to as the Phlogopite Peridotite unit, Ph-Pd) crop out as a lens shaped body about 12 km long and 1.5 km wide with a SW-NE strike (Figure 1a,b). They are surrounded by mafic-ultramafic lithologies, which compose the Finero Mafic Complex. The latter is subdivided into three crustal units: (1) the Layered Internal Zone (LIZ), which is structurally the lowest unit, resulting in contact with the Ph-Pd; (2) the Amphibole Peridotite (Amph-Pd) and (3) the External Gabbro (EG). The EG is in contact with metamorphic rocks of the Kinzigite Formation (Figure 1a,b) [17–19,21–25]. The mantle unit and the Finero Mafic Complex are bounded at N-NW by the Insubric line (IL, Figure 1a), which marks the contact of the lower crust and mantle units of the Adria plate with an accretionary prism of the Alpine orogeny (the Austroalpine terrain).

The Ph-Pd unit is mostly composed by spinel harzburgites. Dunite, lherzolites, wehrlites, and pyroxenites are minor lithologies and occur mainly as layers/lenses. Pegmatites and pods with pargasite and phlogopite are common, as well as zircon-bearing felsic dykes that have been dated at Triassic–Jurassic time [26,27]. Chromite-rich layers/pockets mainly occur in dunite, where they are broadly parallel to the high-temperature (HT) foliation [19]. In recent decades, the deformation processes within the mantle peridotites (Ph-Pd) and mafic/ultramafic rocks of the Finero Mafic Complex were the subject of multiple microstructural [1,2,14–16,28–33] and geochemical/geochronological studies [17–25,27,33,34]. According to Tommasi et al. [16] the mantle peridotite experienced a pervasive HT deformation in the presence of hydrous melts with crystallization of pargasite at T of about 980–1080 °C and P <2 GPa. The presence of hydrous melts strongly changed the deformation processes in the upper mantle resulting in rheological weakening, allowing pervasive deformation of the peridotites under low stress conditions (<10 MPa).

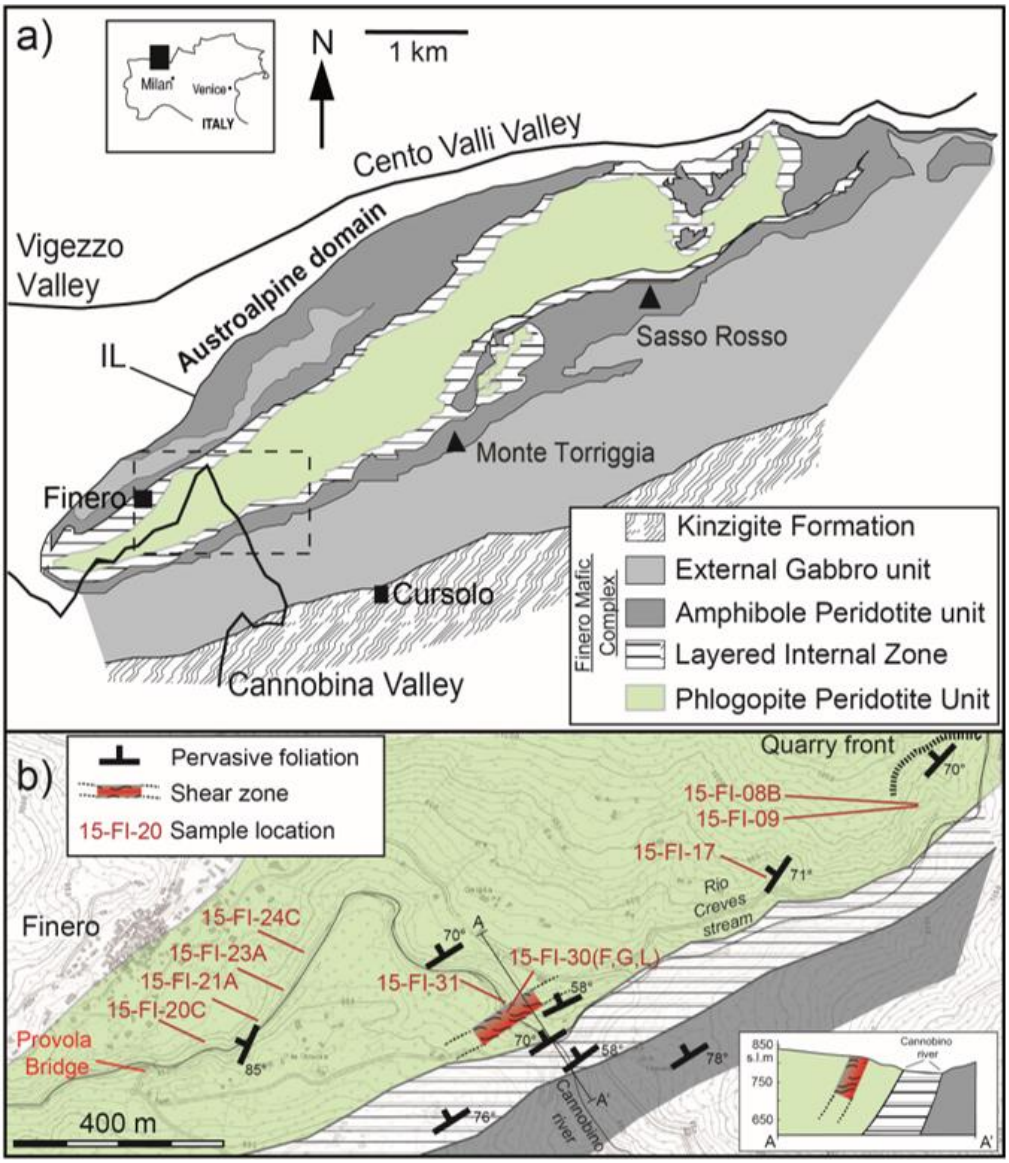

Figure 1. (**a**) Geological map of the northern sector of the Ivrea-Verbano zone showing the main units of the Finero Complex, as well as the Insubric Line (IL) and the Kinzigite Formation, which bounds it to the NW and SE, respectively. (**b**) Sketch map of the area east/northeast of Finero village showing representative attitudes of pervasive foliation and location of samples used for petrography, microstructures, and chemistry (red labels; modified after Tommasi et al. [16]). The studied shear zone is also shown as well as a schematic geological cross section (bottom right).

In addition to this pervasive low-stress deformation, the HT foliation of Finero peridotites is crosscut by many metric-scale shear zones (Figure 1b), recording localized deformation under subsolidus, higher stress conditions [16]. Most of these shear zones are subparallel to the pervasive HT foliation. Matysiak and Trepmann [32] focused on the deformation mechanisms of olivine from mylonitic peridotites from both the Finero Mafic Complex and the Ph-Pd body. They reported that mylonitic deformation occurred at least in two discrete cycles at decreasing temperature (from granulite- to amphibolite-facies) during the pre-Alpine exhumation. Brodie [1] and Altenberger [15] analyzed the bulk chemistry and major element compositions of minerals from mylonites/ultramylonites in the shear zone studied in this work. They argued that deformation was accompanied by mass transport and volume changes and proposed that changes in major element mineral chemistry tend to reflect the bulk chemical variations.

3. Results

3.1. Sampling and Petrography

Samples were collected in three different areas (see Figure 1b for sample location and Table 1; [16]). Coarse-grained ultramafics were sampled along the private road to a quarry front located on the right flank of the Creves stream valley (samples: 15-FI-08B, 15-FI-09, 15-FI-17) and along the Cannobino river, downstream of the Provola bridge (15-FI-20C, 15-FI-21A, 15-FI-23A, 15-FI-24C), whereas proto- to ultramylonites were sampled in a metric-scale shear zone exposed close to the Cannobino-Creves confluence (15-FI-30F and 15-FI-30L ultramylonites, 15-FI-30G mylonite, and 2 meters away from the shear zone 15-FI-31 protomylonites). Selected samples are representative of the lithologic variability of the Ph-Pd unit (i.e., harzburgite, dunite, lherzolite, and pyroxenitic veins) and of the main microstructures across the shear zone (Figures 2–4). For the sake of simplicity, the samples will be hereafter indicated only by the last part of its label: e.g., 15-FI-30F will be reported as (30F).

Table 1. Labels, GPS coordinates (WGS84), lithologies of samples, and relative symbols used in diagrams.

GPS Coordinates	Sample Name	Lithology	Symbol
N46°06′17.88″/E8°32′36.22″	**15-FI-30F**	Ultramylonite porphyroclasts, matrix	○ ◑
	15-FI-30L		● ◐
	15-FI-30G	Mylonite porphyroclasts, matrix	
N46°06′18.79″/E8°32′35.70″	**15-FI-31**	Protomylonite	□
N46°06′22.44″/E8°32′18.16″	**15-FI-24C**	Harzburgite with pyroxenite vein	■
N46°06′16.38″/E8°32′08.57″	**15-FI-20C**		■
N46°06′19.79″/E8°32′16.29″	**15-FI-23A**	Dunite	+
N46°06′26.90″/E8°32′59.37″	**15-FI-17**		+
N46°06′17.51″/E8°32′12.99″	**15-FI-21A**	Ol. Websterite	×
N46°06′32.16″/E8°32′12.16″	**15-FI-09**	Wehrlite	◇
	15-FI-08B	Lherzolite	▲

3.1.1. Coarse-grained Ultramafics

The coarse-grained ultramafics (Figure 2) are equigranular. The harzburgite (e.g., sample 20C and 24C) is composed by olivine (60–90% vol.%), orthopyroxene (5–20% vol.%), clinopyroxene (0–10% vol.%), chromium-rich spinel (0–1% vol.%), pargasite (0–10% vol.%), and phlogopite (5–10% vol.%). The hydrous phases are distributed in a pervasive way but may also form local enrichments (pockets). Their orientation defines the HT foliation (Figure 2a,b). Phlogopite and amphibole-bearing orthopyroxenite (e.g., 20C, 24C) and Cr-diopside websterite lenses (mm to tens of cm-wide; e.g., 09, 21A) are associated with the harzburgite, defining a compositional layering parallel to the foliation. Locally, in the proximity of websterites, the ultramafics may have a lherzolitic composition (e.g., 08B). Dunites (e.g., 17, 23A) are present as tens of centimeters to several meters thick lens-shaped bodies, mainly elongated parallel to the harzburgite foliation [16]. Dunites may contain phlogopite veins/pods, phlogopite-bearing amphibole pyroxenites, pegmatoidal websterites, and chromitite layers [17–19]. Compared to the harzburgites, dunites are usually enriched in phlogopite (Figure 2b) and depleted in pargasite.

Olivine grains are euhedral to subhedral (Figure 2c), show undulose extinction, and often form triple junctions at 120°. The grain size in the ultramafics increases with olivine content, i.e., in dunites, olivine is very coarse-grained with polygonal and equiaxed shapes (5 mm on average), whereas in pargasite or phlogopite-rich harzburgites and lherzolites olivine crystals are smaller (1.7 mm on average).

Orthopyroxene has very irregular, interstitial-like shapes with cusp-like terminations at triple junctions (Figure 2d–f), except in the coarse websterite layers, where it shows a granular texture. Grains sizes are highly variable, from 50 μm to 1 cm. Coarse orthopyroxene grains may display kink bands and/or undulose extinction.

Clinopyroxene occurs as an interstitial, minor constituent of both harzburgites and dunites (Figure 2e), where it is usually heterogeneously distributed. The grain size is highly variable, from 100 μm to 5 mm. The clinopyroxene abundance tends to be inversely proportional to the amount of pargasite.

Pargasite is usually dispersed within the harzburgite but may also be enriched within diffuse lenses or layers elongated parallel to the harzburgite foliation. It occurs either as subhedral crystals or as more irregularly shaped grains. Grain sizes are on average around 800 μm but may vary from 140 μm to 3 mm.

Phlogopite usually occurs as large flakes, up to 5 mm long, aligned in the foliation (Figure 2e). Phlogopite content is highly variable, usually <5 vol.%. It is mostly undeformed, but locally phlogopite crystals may show undulose extinction, be bent, or display kinks outlined by the cleavages (Figure 2e).

Spinel occurs as an interstitial phase or as subhedral grains among major minerals. It is also a common inclusion within olivine, orthopyroxene, and phlogopite.

3.1.2. Sheared Peridotites

The studied shear zone is well exposed about 50 meters upstream to the confluence between the Cannobino river and Creves stream (Figure 1b). It has an asymmetric structure, being composed by a meter-thick ultramylonitic band and a ca. 3 m-thick mylonitic to protomylonitic zone (Figures 1b, 2 and 3a). Variably deformed felsic dykes were observed within the protomylonites (Figure 3b).

The present work focused on four samples representative of the protomylonites and ultramylonites from this shear zone (Figures 3 and 4). More petrographic and microstructural data from the same shear zone were reported by Brodie [1] and Altenberger [15].

The protomylonite (31), which was collected three meters away from the ultramylonitic zone, represents the less deformed sample. Recrystallization is limited and affects mainly olivine and orthopyroxene (see Figure 3c,d and Figure S1a). Olivine porphyroclasts show a strong shape-preferred orientation, undulose extinction, and closely spaced subgrains boundaries. The olivine recrystallized area fraction is around 21%, and recrystallized grain sizes are about 130 μm. Pyroxene porphyroclasts have irregular shapes and highly indented grain boundaries filled by olivine. Orthopyroxene also occurs as fine-grained interstitial crystals interleaved with recrystallized olivine. Pargasite is abundant (about 11 vol. %); phlogopite is less abundant (<2 vol. %). Both hydrous phases are weakly deformed; they show undulose extinction but no recrystallization (Figure 3c,d and Figure S1a).

The sample (30G) is representative of the transition from protomylonitic to ultramylonitic texture and is therefore heterogeneous at the thin section scale. Half of the thin section is a mylonite characterized by coarse-grained olivine, orthopyroxene, clinopyroxene, and chromite and is more enriched in phlogopite than the protomylonite (31). The other half is an ultramylonite characterized by large porphyroclasts of olivine and orthopyroxene or medium to coarse-grained mineral aggregates surrounded by a fine-grained matrix. Olivine porphyroclast dimensions vary from a hundred of micrometers to millimeters (Figures 3e and 4e). They are characterized by strong undulose extinction and closely spaced subgrains boundaries. The fine-grained matrix consists mainly of phlogopite and olivine with minor ortho- and clinopyroxene, chromite, and secondary antigorite (Figure 4a,b). Grain size in the matrix is in the range of 25–50 μm. Rarely, dolomite, calcite, and apatite were observed within the mylonitic matrix, interlayered with phlogopite and, within fractures of the porphyroclasts, together with serpentine (Figure S1b).

The ultramylonitic samples (30L and 30F) are characterized by rounded, sometimes angular, porphyroclasts of olivine, orthopyroxene, and, rarely, clinopyroxene embedded within a very fine-grained matrix. Both samples show local overprint of late brittle deformation. The number

of porphyroclasts is highly variable and their dimensions vary from a hundred of micrometers to millimeters (Figures 3g–l and 4). The fine-grained matrix surrounding the porphyroclasts has grain sizes in the range of 5–25 µm and is mainly made of phlogopite, olivine, orthopyroxene, clinopyroxene, and secondary antigorite, as well as minor chromite and amphibole (Figures 3g–l and 4).

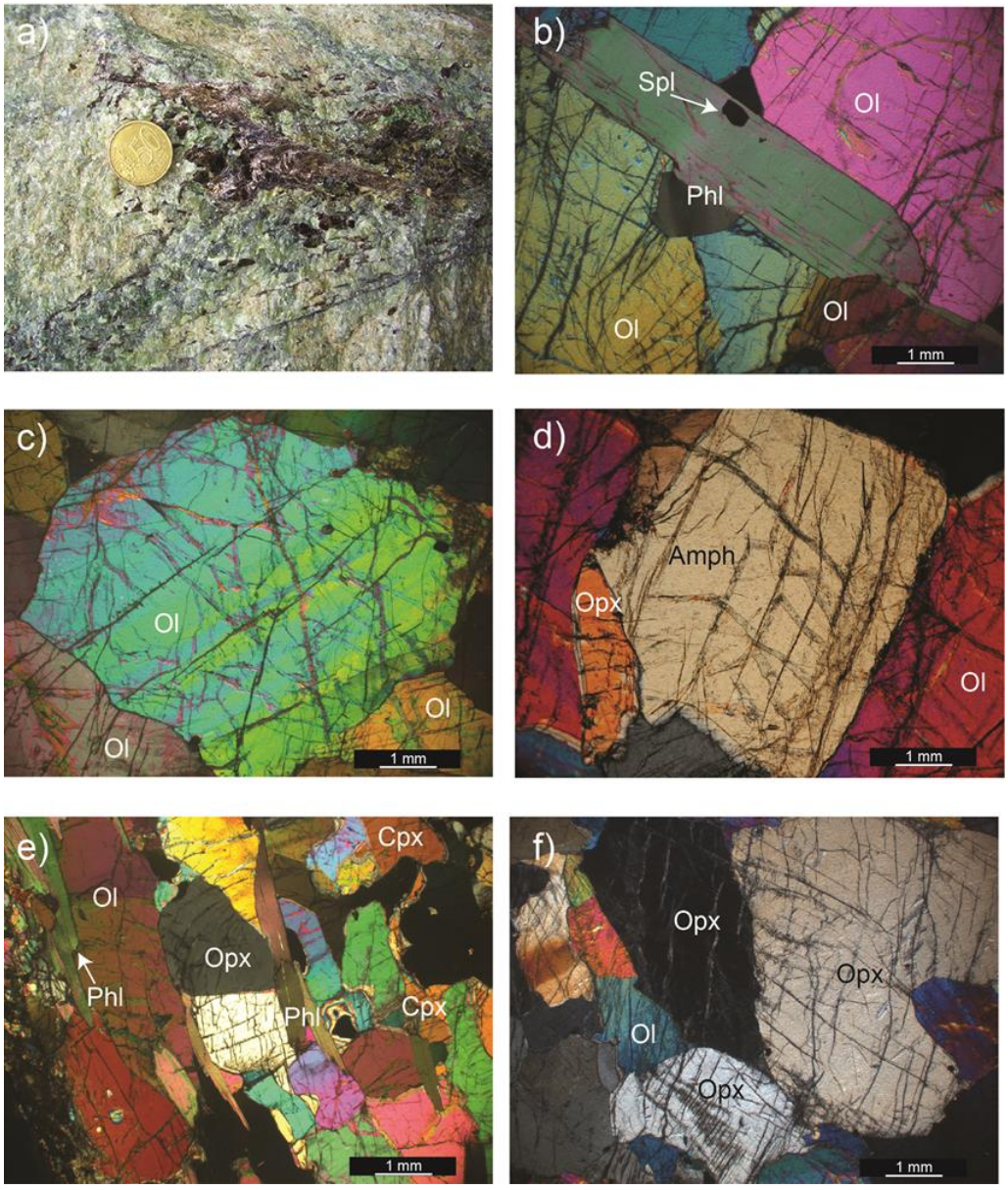

Figure 2. Petrographic and microstructural features in the coarse-grained ultramafic samples of the Ph-Pd unit (crossed polarizers). Mineral abbreviation after [35]. (**a**) Harzburgite at mesoscopic scale: pocket with large flakes of phlogopite (dark-brown), olivine (pale green), Cr-diopside (emerald green), and pargasite (dark spots); (**b**) Typical phlogopite (phl) elongated grain surrounded by olivine (ol) crystals in dunite (17); (**c**) Very coarse olivine grains with polygonal, equiaxed shape in dunite (17); (**d**) Very coarse amphibole grain with polygonal shape surrounded by olivine crystals in harzburgite (20C); (**e**) Mineral assemblage characterized by rounded crystals of orthopyroxene, olivine, and elongated phlogopite crystals, which mark the foliation in lherzolite (08B); (**f**) Anhedral orthopyroxene grain with cusp-like terminations in harzburgite (24C).

Under the optical microscope, the fine-grained matrix from ultramylonites shows an overall brownish colour characterized by alternating lighter and darker layers. Petrographic and chemical

observations by scanning electron microscopy (SEM) and electron microprobe analyses (EMPA) revealed that the widths of the layers vary from few μm up to 500 μm and that the darker layers are richer in phlogopite with respect to the lighter ones, which are mainly composed by olivine and orthopyroxene (Figure 4a–d).

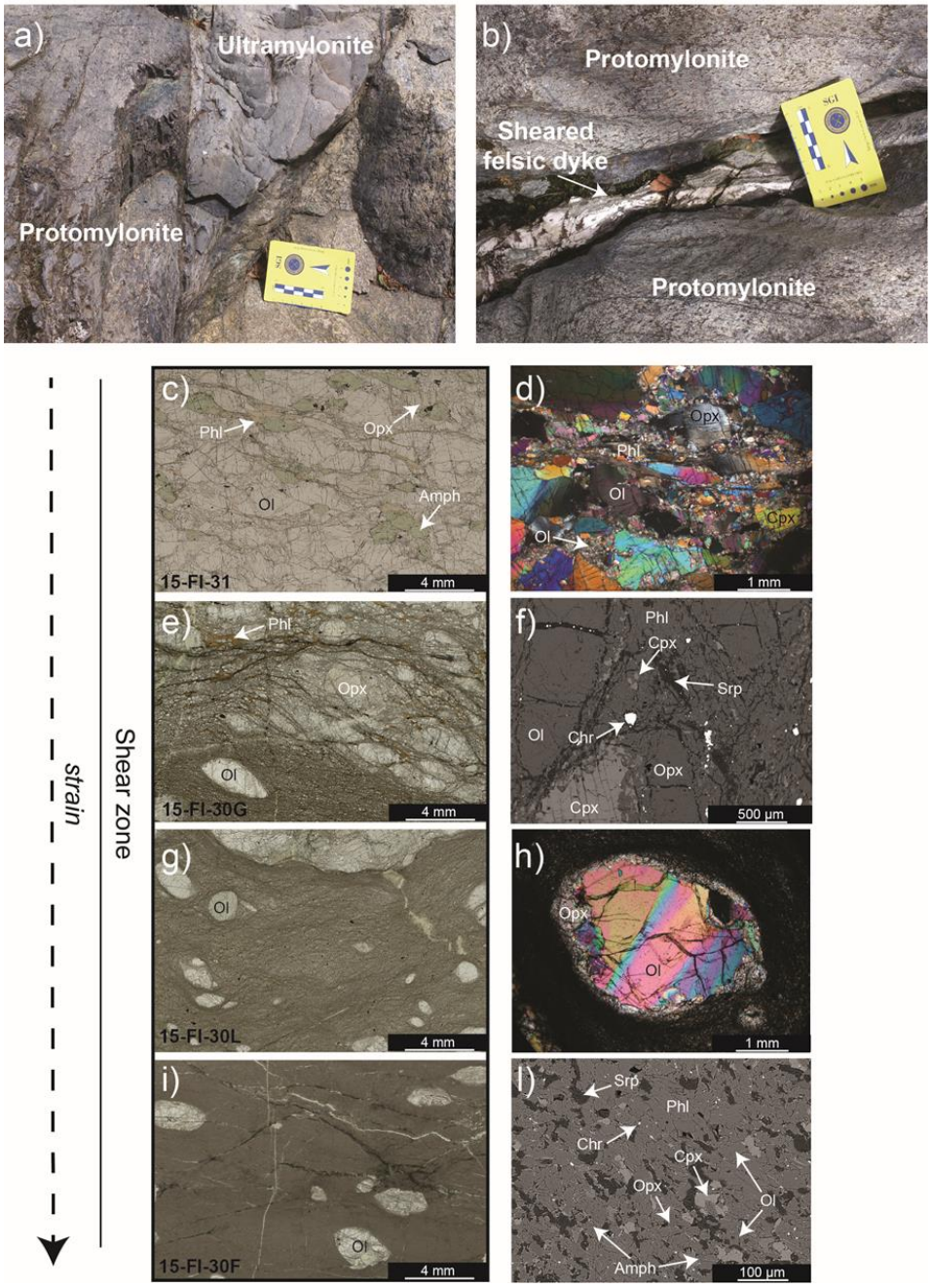

Figure 3. Shear zone macroscopic, petrographic, and microstructural features: (**a**) outcrop picture showing the textural variation from proto- to ultramylonite; (**b**) sheared felsic dyke within protomylonites; (**c**,**e**,**g**,**i**) Clippings of thin section natural light scans, the white box locates the higher resolution images presented on the right; (**d**) Cross-polarized light photomicrographs of protomylonitic harzburgite (31) characterized by elongated olivine and pyroxenes porphyroclasts surrounded by anastomosed seams of a fine-grained matrix; (**f**) Back-Scattered Electron (BSE) image of the mylonitic texture (30G); (**h**) Undulose extinction in a olivine porphyroclast surrounded by orthopyroxene recrystallized grains in the ultramylonite (30L); (**l**) BSE image of the ultramylonitic matrix (30F).

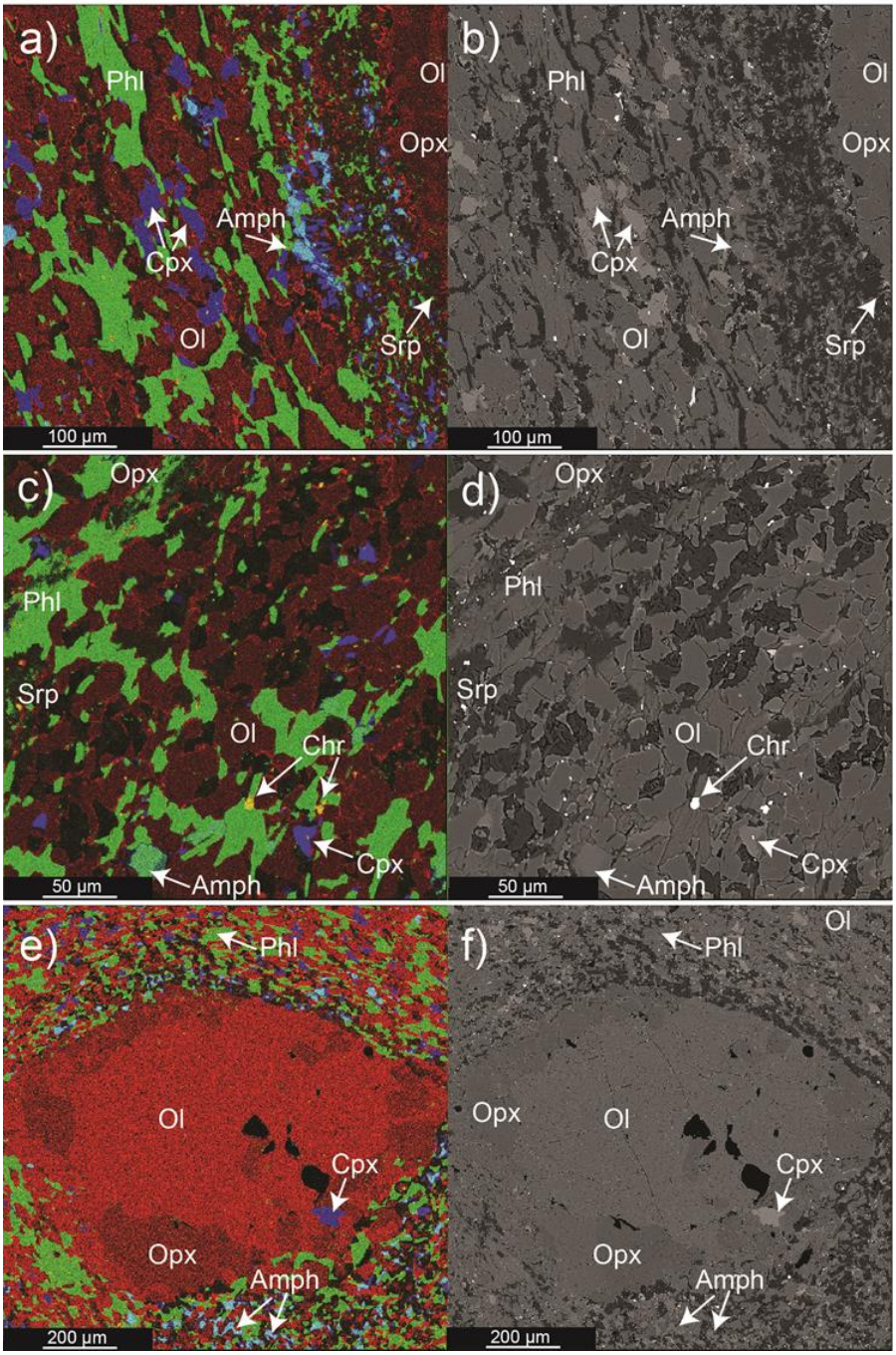

Figure 4. Red, green, and blue (RGB) compositional maps (left side) and BSE images (right side) showing the textures and major element distribution in mineral phases in mylonitic and ultramylonitic samples (30F, 30G, 30L). RGB map colours: Red = Fe; Green = Al and Blue = Ca. (**a**,**b**) texture variation in mylonite (30G) from olivine porphyroclast (on the right) to mylonitic matrix; (**c**,**d**) detail of ultramylonitic matrix (30F); (**e**,**f**) olivine porphyroclast embedded in the ultramylonitic matrix (30F).

Carbonates, apatite, talc, and pentlandite are accessory minerals observed in veins and fractures along the porphyroclasts and within the ultramylonitic matrix. Zircon was detected only within the fine-grained matrix of one ultramylonitic sample (30F). Except for low-temperature secondary minerals, such as talc and serpentine, all accessory minerals observed within both mylonites and ultramylonites have been already described as accessory within the host ultramafic rocks [17,26,36–40].

3.2. Mineral Chemistry

3.2.1. Major Elements

Combining field observations with textures and mineral assemblages, samples were subdivided into two main categories: samples from the shear zone and coarse-grained ultramafics. The shear zone ("shear zone" on diagrams) is further subdivided into a high strain zone, i.e., the ultramylonites (30L, 30F) and mylonite (30G) and a low strain zone, i.e., the protomylonitic sample (31), at the transition with coarse-grained harzburgites. The coarse-grained ultramafics are subdivided into: harzburgites ("harzb." on diagrams; samples 20C, 24C) and "minor ultramafics", which encompass the less abundant dunites, lherzolites, and pyroxenites (samples 08B, 09, 17, 21A, 23A). Data are reported in Table 2 and analytical details in Appendix A.

The forsterite content in olivine ranges between 89.5% and 91.5% (Figure 5a). The Mg# of orthopyroxene (Mg# = [molar $Mg^{2+}/(Mg^{2+}+Fe^{2+}_{tot})$]) ranges between 0.90 and 0.92 (Figure 5b). Clinopyroxene is diopside with Mg# ranging from 0.93 to 0.95 (Figure 5c). The Mg# of clinopyroxene is inversely correlated with its modal abundance, i.e., lherzolite and olivine websterite show the lowest Mg#. Amphibole is dominantly pargasite with Mg# in the range of 0.89–0.92 (Figure 5d), in the sheared peridotites it shows higher edenite component and, locally, higher Cr_2O_3 becoming chromium-pargasite. Phlogopite occurring both as large deformed flakes and small grains within the were observed between core and rim analyses nor between porphyroclasts and matrix-forming grains. However, the Mg# of olivine and orthopyroxene from the ultramylonitic sample with less porphyroclasts (30F) are slightly lower than those reported for other rock types (Figure 5a,b) and even lower than the compositional field defined by previous studies of the shear zone [1,15] and of the coarse-grained ultramafics [17,25].

Spinel in the ultramylonites shows higher Cr# (0.7–0.8; Cr# = [molar $Cr^{3+}/(Cr^{3+}+Al^{3+})$]) and lower Mg# (0.1–0.3) than less deformed protomylonite and coarse-grained harzburgites, which display Mg# and Cr# between 0.3 and 0.45 and 0.4 and 0.7, respectively (Figure 5f).

The Al_2O_3 content (wt.%) in orthopyroxene, clinopyroxene, amphibole, and phlogopite from the mylonite (30G) and ultramylonitic samples (30L, 30F) is distinctly lower that in the other rock types, i.e., the protomylonite (31) and coarse-grained harzburgites and minor ultramafics (Figure 6a,b). For instance, the Al_2O_3 content of orthopyroxene decreases from 1.0–1.5 wt.% to 0.3–0.5 wt.% (Figure 6a and Figure S2a). Amphibole and phlogopite within the protomylonite and coarse-grained harzburgites have Al_2O_3 contents in the range of 11–13 wt.% (Figure 6b) and 15–16 wt.% (Figure S2b), respectively. Within the shear zone, amphibole and phlogopite show lower Al_2O_3 contents in the range of 8–10 wt.% (Figure 6b) and 13–15 wt.% (Figure S2b), respectively.

TiO_2 (wt.%) contents of amphibole and phlogopite outside the high strain portion of the shear zone are in the range of 0.4–0.8 wt.% and 0.5–1.3 wt.%, respectively, distinctly lower than those measured in amphibole (0.6–1.2 wt.%) and phlogopite (1.5–1.7 wt.%) in the high strain zone (Figure 6c,d).

Cr_2O_3 content (wt.%) for orthopyroxene and amphibole from the high strain zone is on average slightly lower with respect to the same minerals within coarse-grained ultramafics (Figure S2e,f). The Cr_2O_3 concentration in orthopyroxene is generally in the range of 0.15–0.45 wt.% outside the high strain zone, whereas it is, on average, lower than 0.25 wt.% within it. The Cr_2O_3 content in amphibole also decreases within the high strain zone; it varies from 1.6–2.1 wt.% within coarse-grained ultramafics to 1.2–1.7 wt.% in the shear zone. Orthopyroxene and amphibole from the transition between the shear zone and coarse-grained harzburgites (i.e., sample 31) show a large variation of Cr_2O_3, overlapping values from both the shear zone samples and the coarse-grained ultramafics (Figure S2e,f). Clinopyroxene has Cr_2O_3 content in the range of 0.2–0.8 wt.% without clear variations among samples (Figure S2g). Phlogopite is characterized by a Cr_2O_3 content of 1.0–1.4 wt.% showing a weak decreasing trend from coarse-grained ultramafics towards the high strain domain of the shear zone (Figure S2h).

Na_2O and K_2O in amphibole vary significantly between the high strain domain of the shear zone and outside, showing opposite trends (Figure 6e,f). The Na_2O content of coarse-grained lithologies and of the protomylonite (31) is in the range of 2.0–2.5 wt.%, whereas within the high strain domain of the shear zone it is generally higher than 2.5 wt.%; with maximum values up to 3.0 wt.% in ultramylonite 30L (Figure 6e). The K_2O content of amphibole in the high strain zone is generally lower (0.4–0.7 wt.%) than the one measured in the protomylonite (31) and coarse-grained lithologies (0.5–1.1 wt.%, Figure 6f). Lower Na_2O and higher K_2O contents were obtained on average from phlogopite analyzed within the ultramylonite with less porphyroclast (30F) with respect to other samples from the shear zone and coarse-grained ultramafics (see Figure S2c,d).

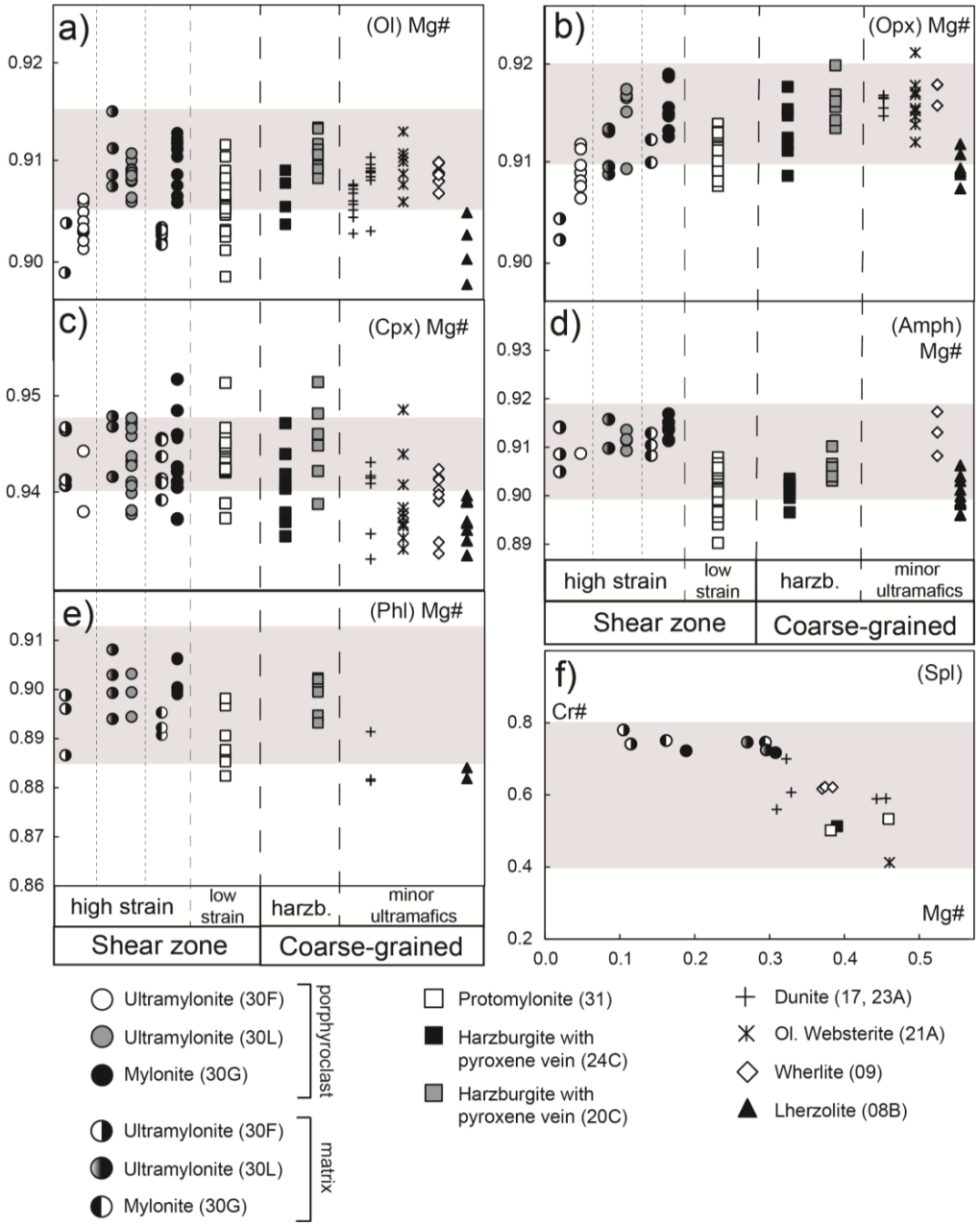

Figure 5. Major element ratios based on EMPA analyses of mineral phases of Finero Ph-Pd samples: Mg# in (**a**) olivine; (**b**) orthopyroxene; (**c**) clinopyroxene; (**d**) amphibole; (**e**) phlogopite; (**f**) Mg# (on x axis) vs Cr# (on y-axis) in Cr-spinel. The grey band refers to the range from literature data [1,15,17] on comparable Finero Ph-Pd samples.

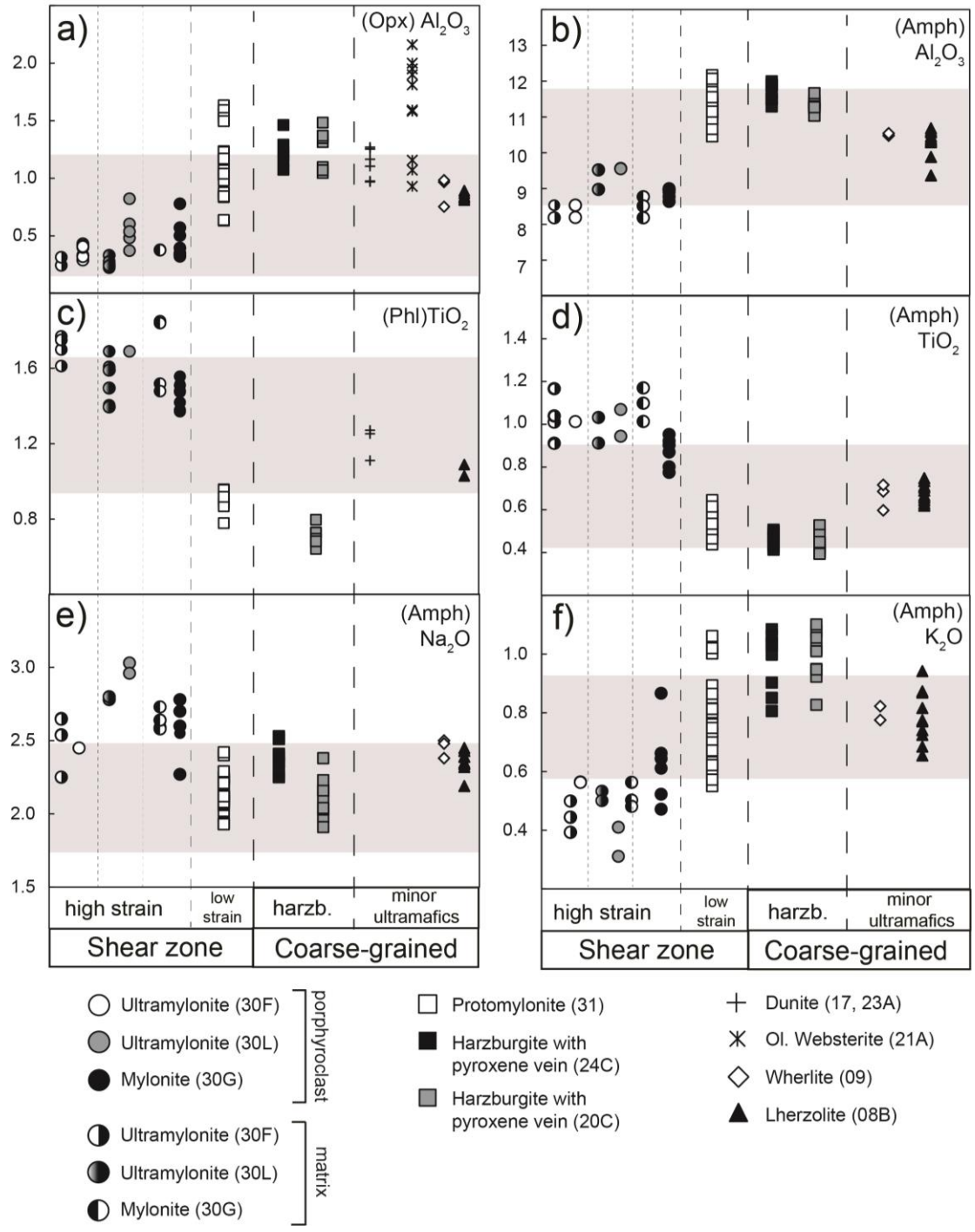

Figure 6. Major element content (wt.%) in mineral phases of Finero Ph-Pd samples: (**a**,**b**) Al_2O_3 in orthopyroxene and amphibole; (**c**,**d**) TiO_2 in phlogopite and amphibole; (**e**) Na_2O and K_2O (**f**) in amphibole. The grey band refers to the range from literature data [1,15,17].

Table 2. Average analyses for major elements (wt.%) of the mineral phases in the Finero ultramafic samples. (FeOt total iron oxide; σ line indicates the standard deviation; N is the number of analysis).

Sample/Lithotype	N	Phase	Texture	SiO_2	TiO_2	Al_2O_3	Cr_2O_3	$FeO_{(t)}$	MnO	NiO	MgO	CaO	Na_2O	K_2O	Total
15-FI-30F	**10**	**Ol**	**porphyroclast**	40.55	0.02	0.00	0.01	9.40	0.11	0.40	49.39	0.01	0.01	0.00	99.91
Ultramylonite		σ		0.425	0.022	0.007	0.012	0.190	0.041	0.050	0.480	0.006	0.012	0.004	
	3	**Ol**	**matrix**	40.92	0.03	0.00	0.02	9.46	0.15	0.40	48.68	0.01	0.01	0.01	99.70
		σ		1.068	0.030	0.008	0.022	0.042	0.025	0.057	1.669	0.014	0.006	0.005	
	7	**Opx**	**porphyroclast**	57.39	0.06	0.33	0.11	6.72	0.17	0.07	34.66	0.25	0.02	0.01	99.79
		σ		0.358	0.033	0.067	0.032	0.228	0.045	0.042	0.215	0.034	0.007	0.005	
	2	**Opx**	**matrix**	57.31	0.05	0.40	0.10	6.53	0.20	0.08	35.08	0.31	0.01	0.00	100.08
		σ		0.863	0.050	0.006	0.014	0.156	0.002	0.098	0.354	0.013	0.013	0.006	
	2	**Cpx**	**porphyroclast**	54.86	0.12	0.65	0.38	1.97	0.06	0.07	17.61	24.66	0.27	0.01	100.65
		σ		0.099	0.096	0.075	0.019	0.163	0.027	0.104	0.042	0.212	0.022	0.009	
	4	**Cpx**	**matrix**	54.57	0.05	0.36	0.27	1.88	0.04	0.03	17.67	24.61	0.26	0.01	99.76
		σ		0.168	0.048	0.056	0.061	0.107	0.012	0.023	0.178	0.172	0.032	0.003	
	1	**Amph**	**porphyroclast**	48.67	0.81	7.46	1.23	3.23	0.05	0.12	20.14	12.07	2.41	0.45	96.64
		σ		1.749	0.245	1.550	0.305	0.303	0.011	0.040	0.881	0.337	0.148	0.102	
	3	**Amph**	**matrix**	46.10	1.10	8.69	1.40	3.60	0.05	0.08	19.62	12.53	2.66	0.47	96.28
		σ		0.502	0.091	0.000	0.120	0.177	0.044	0.060	0.368	0.120	0.014	0.039	
	4	**Phl**	**matrix**	39.79	1.71	13.73	1.02	3.03	0.00	0.17	24.09	0.02	0.38	9.82	93.75
		σ		0.124	0.070	0.399	0.062	0.349	0.000	0.042	0.347	0.018	0.297	0.238	
	2	**Sp**		0.10	0.29	9.25	43.74	39.34	0.58	0.11	2.72	0.03	0.03	0.03	96.23
		σ		0.041	0.101	1.329	0.290	0.806	0.016	0.064	0.141	0.009	0.031	0.002	
15-FI-30L	**11**	**Ol**	**porphyroclast**	40.45	0.02	0.02	0.02	8.92	0.11	0.47	49.58	0.02	0.02	0.01	99.64
Ultramylonite		σ		0.435	0.030	0.016	0.025	0.150	0.023	0.071	0.355	0.021	0.013	0.008	
	5	**Ol**	**matrix**	40.65	0.01	0.00	0.01	9.48	0.15	0.44	48.92	0.01	0.02	0.01	99.68
		σ		0.373	0.016	0.007	0.021	2.211	0.056	0.097	2.206	0.009	0.016	0.007	
	5	**Opx**	**porphyroclast**	56.73	0.08	0.51	0.17	6.13	0.13	0.06	34.43	0.29	0.01	0.00	98.53
		σ		0.792	0.021	0.194	0.095	0.272	0.021	0.046	0.246	0.021	0.013	0.006	
	5	**Opx**	**matrix**	56.70	0.04	0.32	0.09	6.35	0.17	0.07	34.58	0.24	0.01	0.00	98.58
		σ		0.701	0.044	0.160	0.027	0.267	0.020	0.020	0.153	0.027	0.011	0.008	
	12	**Cpx**	**porphyroclast**	53.36	0.10	0.79	0.46	1.88	0.06	0.06	17.25	24.15	0.36	0.01	98.48
		σ		0.571	0.046	0.087	0.120	0.110	0.040	0.051	0.105	0.219	0.040	0.009	
	3	**Cpx**	**matrix**	53.82	0.09	0.62	0.43	1.84	0.07	0.07	17.49	24.22	0.36	0.01	99.02
		σ		0.491	0.054	0.252	0.206	0.121	0.036	0.046	0.709	0.199	0.077	0.011	
	3	**Amph**	**porphyroclast**	45.27	1.31	9.80	1.84	3.25	0.04	0.10	18.79	12.30	2.95	0.38	96.04
		σ		1.034	0.220	0.193	0.208	0.156	0.013	0.020	0.415	0.020	0.080	0.064	
	2	**Amph**	**matrix**	45.57	0.96	9.37	1.51	3.30	0.01	0.14	19.28	12.23	2.79	0.50	95.66
		σ		0.664	0.061	0.266	0.163	0.080	0.025	0.016	0.324	0.089	0.012	0.038	
	5	**Phl**	**matrix**	39.69	1.56	14.47	1.11	2.69	0.02	0.22	24.14	0.03	0.65	9.14	93.70
		σ		0.538	0.110	0.165	0.083	0.151	0.021	0.054	0.412	0.019	0.236	0.384	
	2	**Sp**		0.01	0.32	11.89	49.26	30.88	0.24	0.19	6.84	0.00	0.03	0.01	99.63
		σ		0.000	0.113	0.785	0.629	0.559	0.048	0.049	0.481	0.004	0.004	0.002	
15-FI-30G	**8**	**Ol**	**porphyroclast**	40.80	0.02	0.00	0.01	9.13	0.14	0.40	49.65	0.01	0.01	0.00	100.16
Mylonite		σ		0.359	0.016	0.006	0.010	0.395	0.035	0.045	0.293	0.011	0.007	0.006	
	14	**Ol**	**matrix**	41.15	0.01	0.01	0.01	8.84	0.12	0.42	49.32	0.01	0.01	0.01	99.91
		σ		0.261	0.017	0.013	0.010	0.426	0.029	0.046	0.880	0.017	0.014	0.006	
	5	**Opx**	**porphyroclast**	58.20	0.07	0.48	0.16	6.19	0.13	0.10	34.50	0.28	0.00	0.00	100.10
		σ		0.576	0.036	0.203	0.119	0.232	0.018	0.039	0.475	0.019	0.000	0.005	

Table 2. *Cont.*

Sample/Lithotype	N	Phase	Texture	SiO_2	TiO_2	Al_2O_3	Cr_2O_3	$FeO_{(t)}$	MnO	NiO	MgO	CaO	Na_2O	K_2O	Total
	2	**Opx**	**matrix**	58.29	0.03	0.34	0.08	6.19	0.16	0.08	35.11	0.25	0.00	0.00	100.53
		σ		0.382	0.003	0.028	0.021	0.092	0.033	0.060	0.342	0.033	0.008	0.001	
	9	**Cpx**	**porphyroclast**	54.50	0.10	0.63	0.39	1.94	0.06	0.06	17.37	24.50	0.32	0.00	99.88
		σ		0.412	0.042	0.164	0.136	0.185	0.030	0.039	0.272	0.336	0.081	0.007	
	7	**Cpx**	**matrix**	55.22	0.06	0.60	0.43	1.73	0.07	0.07	17.34	24.80	0.27	0.00	100.59
		σ		0.453	0.012	0.106	0.008	0.099	0.008	0.077	0.283	0.120	0.028	0.002	
	6	**Amph**	**porphyroclast**	47.09	0.90	8.87	1.61	3.25	0.04	0.09	19.43	12.48	2.61	0.61	96.97
		σ		0.597	0.132	0.291	0.141	0.066	0.024	0.035	0.280	0.140	0.169	0.137	
	3	**Amph**	**matrix**	46.92	1.05	8.99	1.40	3.42	0.00	0.07	19.24	12.30	2.60	0.53	96.50
		σ		0.191	0.061	0.092	0.082	0.007	0.004	0.045	0.311	0.035	0.007	0.043	
	6	**Phl**	**porphyroclast**	40.09	1.46	14.35	1.16	2.73	0.02	0.19	24.22	0.00	0.70	9.14	94.06
		σ		0.238	0.229	0.641	0.075	0.503	0.015	0.041	0.422	0.015	0.276	0.112	
	4	**Phl**	**matrix**	40.12	1.60	14.30	1.12	2.94	0.01	0.21	24.06	0.02	0.63	9.10	94.11
		σ		0.238	0.229	0.641	0.075	0.503	0.015	0.041	0.422	0.015	0.276	0.112	
	4	**Sp**		0.05	0.30	11.79	48.43	32.83	0.37	0.10	5.80	0.01	0.04	0.03	99.73
		σ		0.061	0.035	1.190	1.724	2.535	0.127	0.067	1.900	0.009	0.023	0.046	
15-FI-31	**24**	**Ol**		41.64	0.01	0.00	0.02	8.89	0.14	0.41	47.96	0.01	0.01	0.01	99.10
Protomylonite		σ		0.206	0.017	0.005	0.027	0.213	0.028	0.059	0.694	0.011	0.012	0.005	
	22	**Opx**		58.50	0.04	1.12	0.21	6.16	0.15	0.07	33.28	0.31	0.01	0.00	99.84
		σ		0.382	0.031	0.294	0.110	0.117	0.028	0.042	0.434	0.111	0.008	0.005	
	17	**Cpx**		55.74	0.06	0.90	0.27	1.81	0.08	0.05	16.86	24.64	0.17	0.00	100.58
		σ		0.308	0.037	0.186	0.113	0.105	0.025	0.038	0.322	0.156	0.034	0.010	
	28	**Amph**		46.56	0.53	11.43	1.61	3.46	0.04	0.10	17.80	12.52	2.15	0.78	96.98
		σ		0.584	0.056	0.394	0.242	0.129	0.027	0.043	0.450	0.203	0.121	0.148	
	7	**Phl**		40.53	0.90	16.17	1.14	2.78	0.00	0.23	22.44	0.01	0.66	9.17	94.03
		σ		0.405	0.061	0.402	0.113	0.146	0.006	0.061	0.529	0.011	0.065	0.093	
	2	**Sp**		0.00	0.09	24.49	41.69	23.39	0.14	0.08	11.14	0.02	0.01	0.00	101.05
		σ		0.000	0.067	0.948	2.058	2.213	0.018	0.019	1.379	0.012	0.009	0.002	
15-FI-24C	**4**	**Ol**		41.63	0.01	0.01	0.01	8.89	0.12	0.39	48.31	0.02	0.01	0.00	99.41
Harzburgite		σ		0.126	0.012	0.011	0.021	0.178	0.029	0.031	0.698	0.012	0.012	0.001	
	7	**Opx**		58.45	0.02	1.21	0.29	6.01	0.14	0.10	33.31	0.40	0.01	0.00	99.95
		σ		0.212	0.025	0.135	0.102	0.218	0.024	0.018	0.381	0.175	0.008	0.004	
	8	**Cpx**		55.27	0.05	1.28	0.52	1.87	0.07	0.06	16.61	24.27	0.29	0.00	100.29
		σ		0.307	0.033	0.186	0.094	0.128	0.024	0.042	0.155	0.246	0.038	0.004	
	8	**Amph**		46.00	0.45	11.76	1.87	3.46	0.04	0.10	17.68	12.42	2.38	0.97	97.13
		σ		0.287	0.035	0.245	0.150	0.081	0.034	0.055	0.185	0.117	0.101	0.105	
15-FI-20C	**12**	**Ol**		41.22	0.02	0.01	0.01	8.72	0.13	0.40	49.89	0.01	0.01	0.00	100.43
Harzburgite		σ		0.291	0.024	0.012	0.011	0.189	0.032	0.044	0.435	0.006	0.012	0.006	
	8	**Opx**		57.81	0.03	1.26	0.27	6.00	0.13	0.08	34.51	0.37	0.03	0.01	100.50
		σ		0.539	0.020	0.166	0.058	0.135	0.027	0.037	0.286	0.060	0.025	0.008	
	6	**Cpx**		54.75	0.07	1.12	0.38	1.79	0.07	0.03	17.33	24.31	0.19	0.00	100.02
		σ		0.367	0.043	0.275	0.137	0.128	0.014	0.027	0.334	0.413	0.031	0.005	
	10	**Amph**		46.26	0.42	11.40	1.80	3.47	0.06	0.09	18.64	12.51	2.12	0.99	97.75
		σ		0.349	0.041	0.159	0.106	0.066	0.030	0.049	0.203	0.077	0.135	0.083	
	8	**Phl**		40.03	0.70	16.30	1.17	2.68	0.00	0.24	23.80	0.01	0.69	9.16	99.86
		σ		0.370	0.050	0.150	0.050	0.090	0.010	0.040	0.340	0.020	0.020	0.210	
	1	**Sp**		0.15	0.12	24.84	39.04	27.17	0.23	0.13	9.76	0.00	0.00	0.00	101.43

Table 2. *Cont.*

Sample/Lithotype	N	Phase	Texture	SiO_2	TiO_2	Al_2O_3	Cr_2O_3	$FeO_{(t)}$	MnO	NiO	MgO	CaO	Na_2O	K_2O	Total
15-FI-23A	**10**	**Ol**		41.45	0.02	0.01	0.01	9.02	0.15	0.36	50.16	0.01	0.02	0.01	101.22
Dunite		σ		0.293	0.028	0.007	0.020	0.204	0.025	0.033	0.258	0.009	0.021	0.020	
	6	**Opx**		57.99	0.11	1.12	0.26	6.10	0.16	0.04	35.03	0.46	0.01	0.00	101.29
		σ		0.155	0.024	0.131	0.062	0.092	0.029	0.029	0.202	0.075	0.013	0.007	
	2	**Cpx**		55.20	0.16	1.07	0.35	1.95	0.06	0.04	17.72	24.61	0.19	0.02	101.36
		σ		0.042	0.133	0.137	0.072	0.064	0.023	0.049	0.078	0.085	0.012	0.010	
	4	**Sp**		0.14	0.68	19.65	41.60	29.04	0.22	0.14	10.11	0.00	0.03	0.00	101.60
		σ		0.141	0.058	1.015	2.762	4.372	0.054	0.061	1.732	0.002	0.036	0.008	
15-FI-17	**9**	**Ol**		41.58	0.02	0.00	0.01	8.98	0.15	0.34	48.43	0.02	0.00	0.00	99.53
Dunite		σ		0.363	0.021	0.008	0.027	0.134	0.042	0.040	0.395	0.012	0.004	0.005	
	4	**Cpx**		55.52	0.09	0.95	0.64	1.97	0.07	0.03	16.72	23.95	0.43	0.00	100.39
		σ		0.273	0.011	0.157	0.155	0.151	0.049	0.041	0.134	0.308	0.099	0.000	
	3	**Phl**		40.88	1.21	15.30	1.51	2.96	0.00	0.17	22.72	0.00	0.83	9.15	94.73
		σ		0.550	0.088	0.186	0.076	0.127	0.003	0.065	0.297	0.000	0.100	0.229	
	1	**Sp**		0.04	0.45	13.99	48.68	29.02	0.20	0.11	7.75	0.00	0.04	0.00	100.28
15-FI-21A	**8**	**Ol**		41.34	0.02	0.00	0.00	8.86	0.12	0.42	49.65	0.02	0.01	0.00	100.45
Ol. Websterite		σ		0.364	0.026	0.004	0.007	0.224	0.017	0.048	0.515	0.010	0.014	0.005	
	10	**Opx**		57.82	0.03	1.62	0.32	6.10	0.15	0.05	34.44	0.33	0.01	0.01	100.86
		σ		0.393	0.025	0.429	0.144	0.294	0.039	0.032	0.532	0.067	0.013	0.005	
	10	**Cpx**		54.68	0.09	1.73	0.56	1.97	0.08	0.06	16.96	24.39	0.21	0.00	100.72
		σ		0.491	0.023	0.337	0.170	0.124	0.037	0.043	0.283	0.147	0.050	0.005	
	1	**Sp**		0.05	0.20	31.15	32.60	24.81	0.17	0.15	11.87	0.01	0.03	0.00	101.05
15-FI-09	**9**	**Ol**		41.39	0.02	0.01	0.02	8.95	0.14	0.30	49.94	0.02	0.01	0.01	100.78
Wehrlite		σ		0.248	0.030	0.007	0.021	0.142	0.028	0.045	0.292	0.010	0.009	0.007	
	3	**Opx**		58.17	0.08	0.90	0.28	5.94	0.16	0.07	34.61	0.39	0.01	0.01	100.62
		σ		0.274	0.029	0.129	0.018	0.075	0.053	0.018	0.324	0.107	0.009	0.004	
	10	**Cpx**		55.17	0.06	1.12	0.59	2.03	0.07	0.04	17.52	23.71	0.36	0.00	100.67
		σ		0.388	0.033	0.069	0.126	0.158	0.032	0.044	0.544	0.608	0.031	0.007	
	3	**Amph**		47.14	0.65	9.99	1.96	3.24	0.06	0.11	19.09	12.41	2.45	0.58	97.68
		σ		1.318	0.063	1.074	0.196	0.111	0.009	0.031	0.447	0.361	0.064	0.385	
	3	**Sp**		0.05	0.28	18.52	45.07	27.58	0.27	0.06	9.33	0.01	0.01	0.01	101.18
		σ		0.038	0.092	0.214	0.428	0.349	0.026	0.024	0.174	0.011	0.010	0.012	
15-FI-8B	**4**	**Ol**		41.77	0.01	0.01	0.03	9.34	0.12	0.37	47.77	0.00	0.02	0.00	99.45
Lherzolite		σ		0.083	0.011	0.007	0.019	0.242	0.016	0.021	0.571	0.004	0.014	0.003	
	7	**Opx**		58.71	0.05	0.84	0.21	6.30	0.16	0.06	33.41	0.42	0.01	0.00	100.17
		σ		0.185	0.019	0.030	0.033	0.093	0.027	0.037	0.252	0.051	0.009	0.001	
	9	**Cpx**		56.05	0.08	0.95	0.50	1.99	0.08	0.05	16.71	24.31	0.32	0.00	101.04
		σ		0.373	0.040	0.137	0.147	0.049	0.042	0.052	0.240	0.110	0.042	0.003	
	10	**Amph**		47.14	0.67	10.40	1.80	3.56	0.04	0.11	18.02	12.39	2.36	0.78	97.27
		σ		0.490	0.045	0.383	0.162	0.112	0.025	0.035	0.317	0.078	0.075	0.090	
	2	**Phl**		40.84	1.06	15.53	1.29	2.96	0.01	0.20	22.30	0.00	0.82	9.12	94.12

3.2.2. Minor and Trace Elements Concentrations in Porphyroclasts

Trace element analyses of major rock-forming minerals were performed on all rock types and are shown following the rocks grouping defined before, i.e., shear zone (high strain and low strain domains), coarse-grained harzburgites, and coarse-grained minor ultramafics. Average values are reported in Table 3; the whole dataset is available as Supplementary Table S2 (see Appendix A for details in the data acquisition and processing). The small size of the matrix-forming minerals within the shear zone (<20 μm) hampered LA-ICP-MS analysis, which could only be performed on porphyroclasts from both protomylonites and ultramylonites. Single spot analyses were collected in core and rims of porphyroclasts. For selected grains, we also performed core-to-rim transects. Analyses were carried out on several porphyroclasts of olivine, orthopyroxene, and phlogopite but only on few clinopyroxene porphyroclasts due to their lower abundance.

Olivine porphyroclasts from different lithologies and textural types show significant variation in Li, Co, Ni, and Zn contents (Figure 7a–d; Table 3). All these elements have on average higher concentrations (up to three times) within the shear zone with respect to the coarse-grained ultramafics (Figure 7a–d). The concentration of Zn progressively increases towards the core of the shear zone, which is associated with a decrease of the number of olivine porphyroclasts (Figure 7d). The highest Zn values were obtained from the ultramylonitic sample containing only four olivine porphyroclasts (30F) in the studied thin section. In contrast, the maximum concentrations for Li are documented at the transition between the mylonite (30G) and the ultramylonite (30L), as previously documented also for Mg# and Na/K ratios.

In orthopyroxene porphyroclasts, as for olivine, the concentration of Li, Co, Ni, and Zn is on average higher in the protomylonites and ultramylonites than in the coarse-grained ultramafics (Table 3). Orthopyroxenes from the shear zone are also characterized by slightly lower values of Ca, Sc, V, and Cr (Figure 7e–h) but higher values of Ti (Table 3).

The Ti content of clinopyroxene porphyroclasts within the shear zone, especially in the ultramylonites, is significantly higher (>600 ppm) than in the coarse-grained ultramafics, which is <600 ppm. A similar trend is observed for Sc, which is higher (>50 ppm) in ultramylonites than in other rock types (<50 ppm; Figure 8b).

Amphibole porphyroclasts from the protomylonite (31) are characterized by higher Ba concentration (115 ppm on average) with respect to amphibole in the coarse-grained ultramafics (<100 ppm, Figure 8d). The trace element patterns mimic those reported for amphiboles from coarse-grained lithologies, but an overall enrichment in REE and Ba can be noticed (Figure S3). These geochemical features are consistent with those observed for clinopyroxene porphyroclasts (Figure S3) from the ultramylonites (30L and 30F) and the mylonite (30G). Amphibole from a coarse-grained harzburgite (24C) displays the highest Sc and V contents, whereas the lowest Sc and V concentrations are observed in amphiboles from the protomylonite (31; Figure 8c and Table 3). The minor and trace element characterization of phlogopite revealed some systematic variations among samples and textural sites. Phlogopite from the high-strain zone (mylonite 30G) showed the highest Li (up to six times the average values for other samples) and lowest Ba contents (Figure 8e,f).

In order to detect intragranular variations, trace element transects were performed across olivine and orthopyroxene porphyroclasts of samples from the high strain zone (Figure 9). Even though the LA-ICP-MS profiles are coarsely spaced (distance between two spots >100 μm), they show clear geochemical features. The Ni content across olivine porphyroclasts shows opposite trends between ultramylonites and mylonites (Figure 9a): it linearly decreases from core to rims in ultramylonites (30L and 30F) whereas it linearly increases towards the rims in (30G). In this sample (30G), Al and Ti decrease towards the rims (Figure S4). No other significant chemical variations within porphyroclasts from the ultramylonitic samples were observed except for Ti in sample 30F (Figure S4b). Orthopyroxene porphyroclasts in both the mylonite and the ultramylonites show only a weak intragranular chemical variation: Sc slightly decreases from core to the rims (Figure 9b) as well as Al, Ca, Ti, V, and Cr (Table 3).

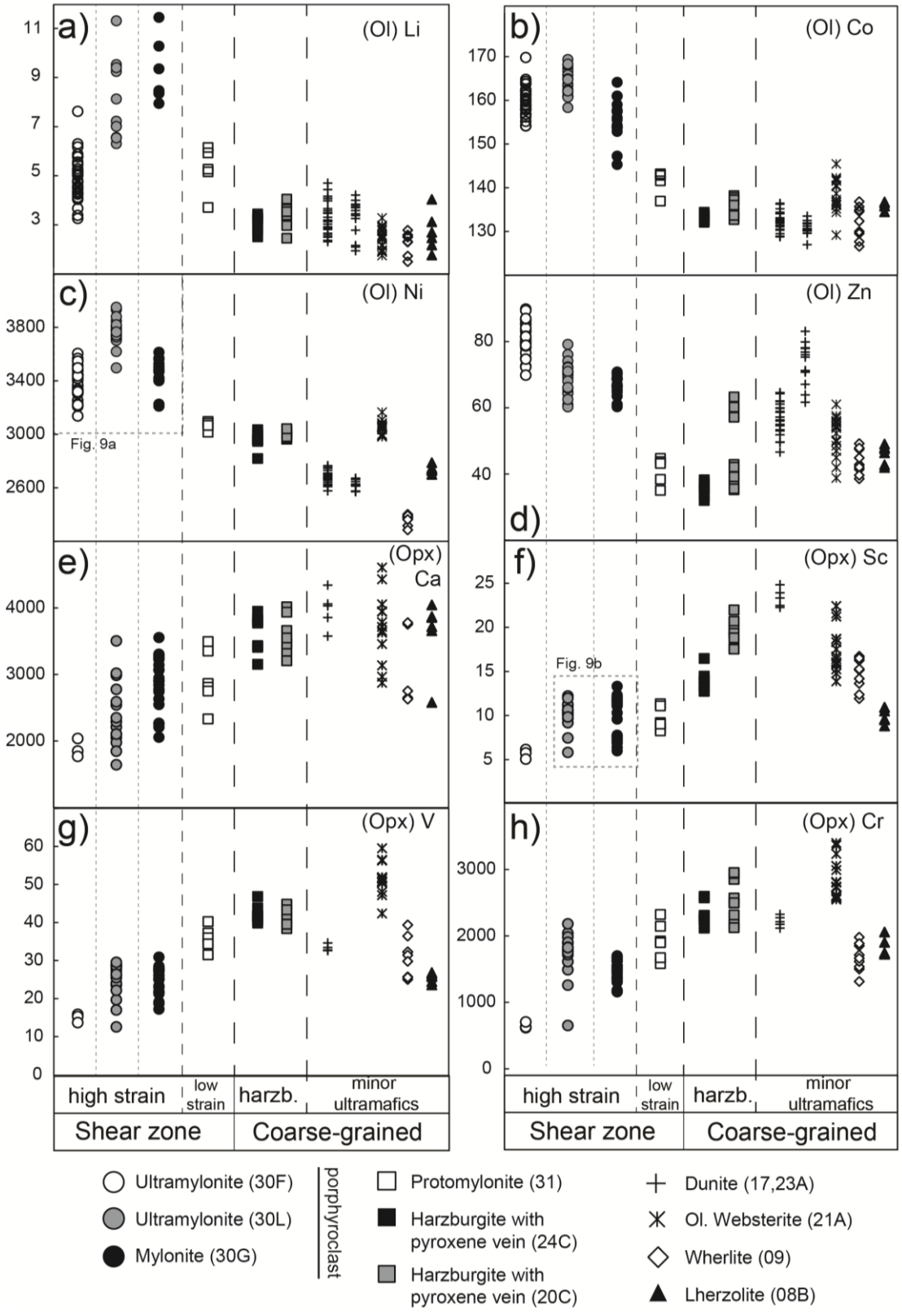

Figure 7. Trace-element concentrations (ppm) in mineral phases of Finero Ph-Pd samples. (**a**–**d**) Li, Co, Ni, Zn content in olivine; (**e**–**h**) Ca, Sc, V, Cr content in orthopyroxene. Dashed boxes in (**c**,**f**) refer to Figure 9a,b respectively.

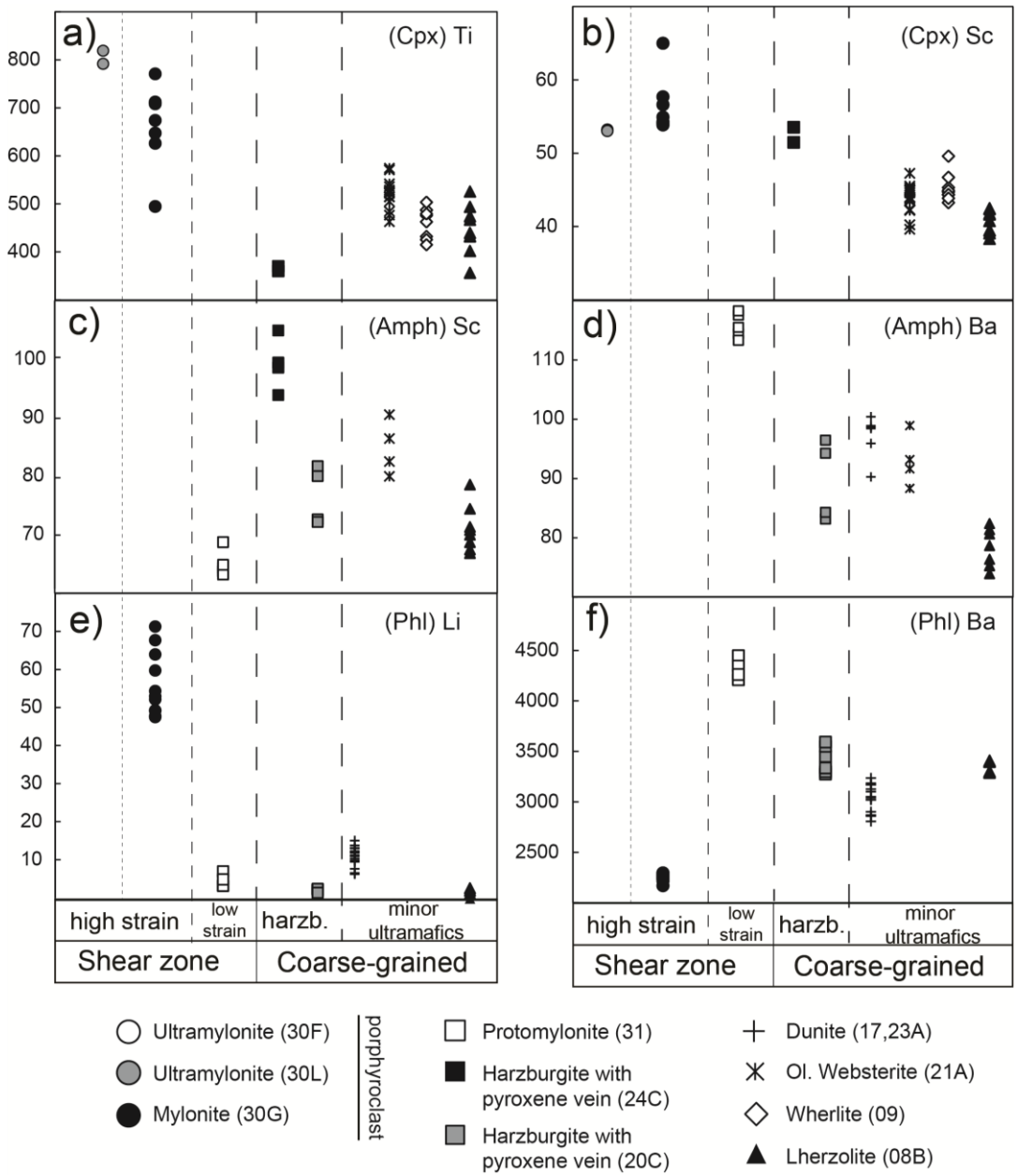

Figure 8. Trace-element concentrations (ppm) in mineral phases of Finero Ph-Pd samples. (**a**,**b**) Al, Sc content in clinopyroxene; (**c**,**d**) Sc, Ba content in amphibole; (**e**,**f**) Li, Ba content in phlogopite.

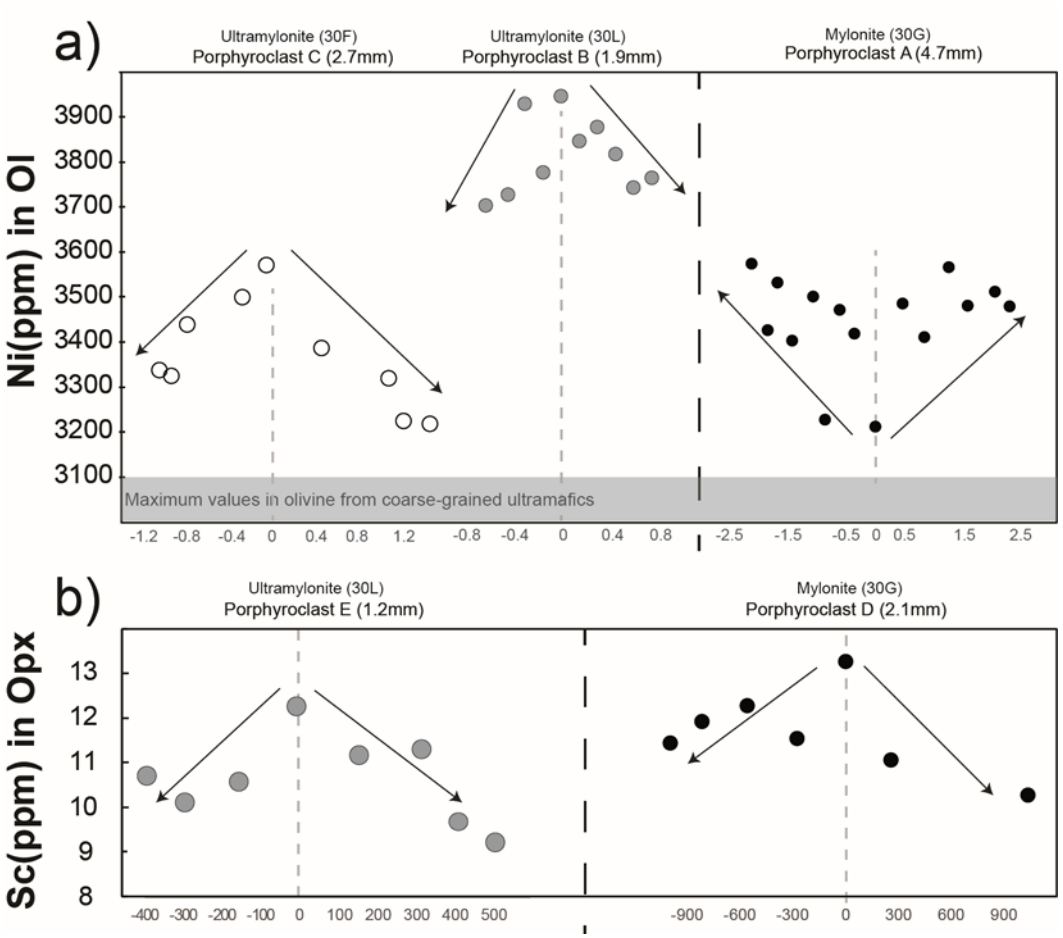

Figure 9. Trace element variation across porphyroclasts from the shear zone. (**a**) Ni (ppm) variation in olivine, and (**b**) Sc (ppm) in orthopyroxene, whose trends are underlined by arrows. X axes: approximate distance (mm in **a** and μm in **b**) from the core (0) towards the rims. The analytical points are largely spaced and not perfectly equidistant due to the presence of fractures and/or inclusions along the crystal avoided during the analytical procedure.

Table 3. Representative average trace element concentrations (ppm) of mineral phases in Finero ultramafic samples.

	Lithotype	Grain	Li	B	Al	Sc	Ti	V	Cr	Co	Ni	Cu	Zn	Rb	Sr	Y	Zr
15-FI-30F	**Ultramylonite**	**Ol**	4.8	17.2	2	1.8	10	0.4	16	158.4	3385	0.2	81.9	0.1	0.2	0.1	0.1
		Opx	1.4	15.4	1663	5.7	345	14.9	651	56.9	631	0.2	61.9	0.3	0.2	0.2	0.0
15-FI-30L	**Ultramylonite**	**Ol**	8.4	16.8	3	2.3	6	0.5	10	164.0	3770	1.2	68.9	0.1	0.4	0.1	0.2
		Opx	5.7	16.7	3235	10.1	489	24.5	1715	53.3	618	1.0	52.4	1.0	0.4	0.4	0.0
		Cpx		24.7	4562	53.1	805	86.3	4424	18.8	334		12.0	224.7	8.3	16.3	0.0
15-FI-30G	**Mylonite**	**Ol**	9.1	20.1	3	2.2	12	0.5	12	155.7	3454	0.6	65.5	0.1	0.1	0.1	0.1
		Opx	5.2	17.8	2800	9.8	539	24.7	1457	54.7	627	0.5	52.3	0.5	0.4	0.5	0.1
		Cpx	5.2	22.4	4141	56.6	662	95.4	4207	19.4	330	0.4	10.2	269.4	7.3	15.4	0.1
		Phl	54.2	25.7	64486	7.9	6717	182.7	7790	47.1	1498	0.9	18.7	105.4	0.1	3.7	5.0
15-FI-31	**Protomylonite**	**Ol**	5.1	9.4	14	1.2	8	0.4	13	142.7	3099		40.2				
		Opx	0.4	15.6	7262	9.6	250	35.7	1924	53.1	598	0.3	43.6		0.2	0.1	0.4
		Amph	1.9	15.3	49543	64.6	3040	281.1	12543	32.5	781	0.2	14.1	6.6	264.0	9.3	37.0
		Phl	4.5	16.4	72399	6.3	5291	180.2	7860	47.8	1618	0.2	16.7	584.7	85.3	0.0	2.3
15-FI-24C	**Harzburgite**	**Ol**	2.8	17.3	3	1.8	5	0.3	10	132.5	2926	0.5	35.5				
		Opx	1.2	16.5	7394	13.9	180	42.2	2313	51.1	601	0.3	37.1		0.2	0.1	0.9
		Cpx	3.3	18.6	7201	52.5	365	100.4	3552	17.1	304	4.7	6.4	0.0	130.4	1.8	17.9
		Amph	1.1	14.9	50698	99.2	2389	343.7	12637	31.2	763	3.9	12.7	8.6	294.6	5.1	73.7
15-FI-20C	**Harzburgite**	**Ol**	3.2	29.2	5	5.9	6	0.4	12	135.6	3003		45.8		0.0	0.0	0.1
		Opx	0.6	20.7	7776	19.5	236	41.8	2547	51.7	626		46.5		0.2	0.1	0.9
		Amph	0.9	29.3	44315	76.7	2373	293.1	12064	31.7	791		12.4	9.0	262.4	4.1	49.1
		Phl	2.0	36.3	64832	12.0	3841	189.4	8259	45.9	1572		20.8	723.4	94.9	0.0	3.7
15-FI-23A	**Dunite**	**Ol**	3.0	42.6	5	8.1	27	0.6	11	130.7	2622		73.3	0.1	0.0	0.0	0.1
		Opx	1.0	33.4	6544	23.4	576	33.2	2221	49.4	532		63.1	0.1	0.1	0.2	1.7
15-FI-17	**Dunite**	**Ol**	3.1	12.8	17	2.5	9	0.3	13	131.4	2703	0.2	58.5	0.1	0.0	0.0	0.0
		Phl	10.8	18.0	66804	9.7	6314	157.5	9408	45.0	1409	0.4	22.2	533.8	137.9	0.0	4.9
15-FI-21A	**Ol.Websterite**	**Ol**	2.2	29.6	11	1.8	10	0.4	8	140.6	3058	3.7	47.4		0.1		0.2
		Opx	1.2	27.7	9265	16.6	267	54.1	3036	56.0	669	0.6	40.9	0.0	0.7	0.1	1.3
		Cpx	2.3	24.9	10141	42.7	547	117.5	4295	20.6	366	0.5	9.7	0.1	99.5	2.4	18.9
		Amph	1.9	6.3	44527	81.3	2523	303.3	11769	30.9	750	1.0	13.2	10.7	279.9	6.3	57.6
15-FI-09	**Wehrlite**	**Ol**	2.1	34.0	19	5.5	12	0.7	13	132.0	2364		43.8	0.1	0.2	0.1	0.2
		Opx	1.8	40.3	4707	14.7	318	30.9	1674	49.9	469		42.2	1.8	5.0	1.0	1.7
		Cpx	1.9	35.6	6063	45.2	463	87.3	4180	19.9	278		9.1	0.1	156.5	1.8	6.9
15-FI-8B	**Lherzolite**	**Ol**	2.5	8.1	4	2.0	9	0.3	10	135.7	2729	0.5	45.8			0.0	0.1
		Opx	0.4	6.6	4788	9.9	297	25.2	1839	51.2	557	0.4	39.0		0.2	0.1	0.3
		Cpx	2.0	8.1	5625	40.7	448	78.8	4405	17.7	299	0.4	6.9		156.2	1.7	6.5
		Amph	1.0	7.2	43009	70.9	3195	253.1	12044	30.3	712	0.6	13.1	6.2	273.7	4.6	34.5
		Phl	1.5	7.7	62723	6.4	5581	158.3	8424	45.2	1451	0.6	17.0	502.5	88.6	0.1	2.0

Table 3. *Cont.*

	Lithotype	Grain	Ce	Nd	Sm	Eu	Gd	Tb	Dy	Er	Tm	Yb	Lu	Hf	Ta	Pb
15-FI-30F	**Ultramylonite**	**Ol**	0.1	0.2	0.2	0.0	0.1	0.0	0.1	0.1	0.0	0.2	0.0	0.1	0.0	0.1
		Opx	0.0		0.0		0.0	0.1	0.0		0.1		0.1	0.0	0.1	0.3
15-FI-30L	**Ultramylonite**	**Ol**	0.1	0.1	0.2	0.1	0.2	0.0	0.1	0.2	0.0	0.2	0.0	0.1	0.0	0.1
		Opx	0.0	0.2	0.1	0.1	0.0	0.2	0.0	0.0	0.2	0.0	0.1	0.0	0.1	0.1
		Cpx	4.5	5.1	1.3	3.2	0.5	2.4	0.4	0.0	0.4	0.0	1.3		0.6	
15-FI-30G	**Mylonite**	**Ol**	0.1	0.2	0.2	0.2	0.2	0.0	1.3	0.1	0.0	0.2	0.0	0.1	0.0	0.1
		Opx	0.0	0.3	0.1	0.2	0.0	0.2	0.0	0.0	0.2	0.0	0.2	0.0	0.1	0.1
		Cpx	4.6	5.6	1.2	3.6	0.4	1.9	0.3	0.1	0.6	0.1	1.1	0.0	1.0	0.1
		Phl	0.0	0.3	0.0	0.2	0.0	0.2	0.0	0.0	0.3	0.1	0.3	0.4		
15-FI-31	**Protomylonite**	**Ol**	0.0						0.1							
		Opx			0.1											0.1
		Amph	30.0	16.6	3.6	0.9	2.6	0.4	2.1	0.9	0.1	0.9	0.1	0.9	0.2	2.2
		Phl		0.0	0.0						0.0		0.0		0.1	4.0
15-FI-24C	**Harzburgite**	**Ol**		0.1					0.0							
		Opx														
		Cpx	6.1	3.9	1.1	0.2	0.6	0.1	0.4	0.1	0.0	0.2	0.0	0.5	0.0	0.8
		Amph	21.8	12.2	2.8	0.6	1.8	0.2	1.1	0.6	0.1	0.7	0.1	2.1	0.2	2.2
15-FI-20C	**Harzburgite**	**Ol**	0.0	0.0	0.2	0.0	0.1	0.0	0.1	0.0	0.0	0.1	0.0	0.1	0.0	0.1
		Opx	0.0	0.2	0.1	0.1	0.2	0.0	0.1	0.1	0.0	0.1	0.0	0.2	0.0	0.1
		Amph	16.8	10.1	2.1	0.6	1.4	0.2	0.8	0.3	0.1	0.6	0.1	1.4	0.2	1.9
		Phl	0.0		0.1	0.1	0.2	0.0		0.0	0.0	0.0	0.0	0.2	0.2	3.8
15-FI-23A	**Dunite**	**Ol**	0.0	0.2	0.1	0.0	0.1	0.0	0.1	0.1	0.0	0.1	0.0	0.0	0.0	0.1
		Opx	0.0	0.1	0.1	0.0	0.1	0.0	0.1	0.1	0.0	0.2	0.0	0.1	0.0	0.3
15-FI-17	**Dunite**	**Ol**	0.0	0.0	0.0	0.0	0.0	0.0	0.0	0.0	0.0	0.0	0.0	0.0	0.0	0.0
		Phl	0.0	0.0	0.0	0.0	0.0	0.0	0.0	0.0	0.0	0.0	0.0	0.1	0.2	3.6
15-FI-21A	**Ol.Websterite**	**Ol**	0.0		0.2		0.1	0.0		0.1	0.0	0.1	0.0			
		Opx	0.1	0.1	0.1	0.0	0.2	0.0	0.1	0.1	0.0	0.3	0.0	0.1		0.1
		Cpx	8.0	5.7	1.3	0.3	0.9	0.1	0.5	0.3	0.0	0.3	0.0	0.6	0.0	0.5
		Amph	22.7	14.6	3.5	0.8	1.9	0.3	1.4	0.7	0.1	0.8	0.1	1.8	0.1	1.9
15-FI-09	**Wehrlite**	**Ol**	0.0	0.2	0.1	0.0	0.1	0.0	0.1	0.0	0.0	0.1	0.0	0.1	0.0	0.1
		Opx	2.0	2.6	1.8	1.4	1.4	1.1	0.9	1.1	1.3	1.9	1.0	0.8	1.1	1.9
		Cpx	7.8	4.4	0.9	0.3	0.7	0.1	0.4	0.2	0.0	0.2	0.0	0.3	0.0	0.7
15-FI-8B	**Lherzolite**	**Ol**													0.0	
		Opx														
		Cpx	7.5	4.4	0.9	0.2	0.6	0.1	0.4							0.6
		Amph	23.1	12.6	2.7	0.7	1.7	0.2	1.1	0.5	0.1	0.5	0.1	1.0	0.1	1.6
		Phl			0.0											2.7

4. Discussion

4.1. P-T Evolution and Geothermometry

Tommasi et al. [16] inferred that the coarse-grained peridotites of Finero (Ph-Pd) experienced a pervasive high temperature deformation in the presence of a hydrous melt (Figure 10) at P <2.0 GPa and temperature in the range of 1050–1080 °C. These estimates were based on the stability field of pargasite + hydrous melt in the presence of spinel. The high temperature foliation of the peridotite is crosscut by several melanocratic to leucocratic dykes and veins. Giovanardi et al. [25,41], suggested equilibrium T for sapphirine-bearing gabbroic dykes mostly between 980 and 1030 °C at a pressure of 1.0 GPa.

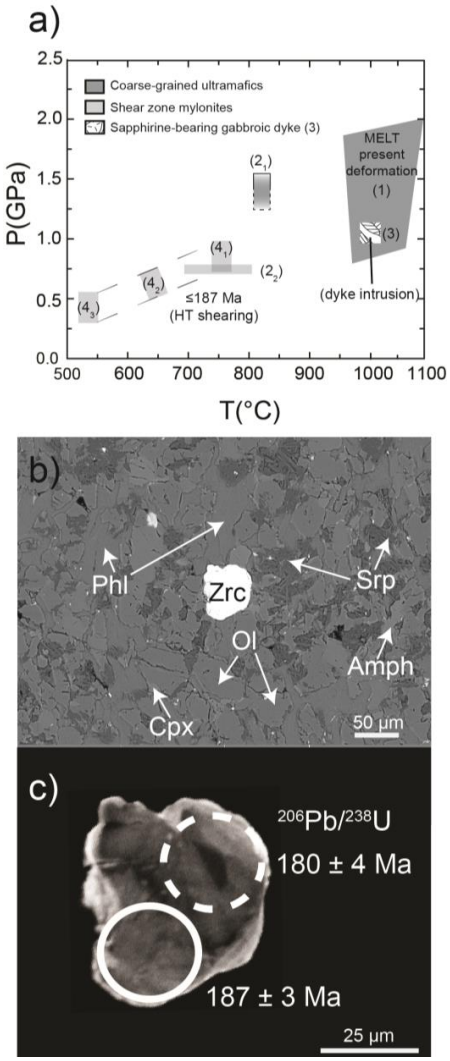

Figure 10. (**a**) Pressure–temperature diagram showing the main conditions for Finero mantle sequence lithologies: (1) the dark grey box defines the melt-present pervasive HT deformation for the coarse-grained ultramafics [16]; (2) P-T results from this study refer to: **(2_1)** subsolidus re-equilibration conditions for the coarse-grained ultramafics; **(2_2)** deformation in the shear zone based on synkinematic minerals; (3) P-T equilibrium conditions for sapphirine-bearing gabbroic dyke [25]; (4) shearing P-T conditions by [15], **(4_1)** = granulite facies; **(4_2)** = amphibolite facies; **(4_3)** = green-schists facies. See text for more details and Table 4. (**b**) BSE image showing the zircon grain within the fine-grained matrix of the ultramylonite (30F); (**c**) zircon CL image showing the zoning features and location of the two LA-ICP-MS pits yielding one concordant (white circle) and one discordant (dashed circle, ^{206}Pb/^{238}U) age.

The pervasive high temperature deformation was followed by localized deformation events that occurred at lower temperatures from granulite to upper greenschist facies conditions (Figure 10a) [1,15,16,28,29,32,42]. The shear zone studied here was formed during one or more of these events, e.g., [15]. Temperatures for the studied samples were estimated by using geothermometers based on the pyroxene solvus. The calibration of Wells [43] for the two-pyroxene geothermometer was used for a direct comparison with existing T estimates for the mylonites obtained with the same calibration, i.e., Brodie [1] and Altenberger [15]. Results are listed in Table 4 and Table S4 and shown in Figure 10a. A pressure of 1.5 GPa (central value of the range proposed by Tommasi et al., [16]) was considered for the coarse-grained ultramafics, 0.75 GPa (from Altenberger [15]) for mylonites s.l. pairing synkinematic pyroxenes (Table 4, Figure 10a). By using the calibration of Wells [43], temperatures range from 815 to 830 °C for the coarse-grained ultramafics and from 680 to 810 °C for the proto- and ultramylonites (Table 4, Figure 10a). Temperatures were also constrained using the Ca-in-Opx geothermometer [44], which points to a smaller interval for the proto- and ultramylonites (670–690 °C; Table 4). Single-element geothermometers for olivine (i.e., Al-in, Cr-in, and V-in olivine geothermometers; [45,46]) systematically provide lower T than two-pyroxene geothermometers (Table 4), presumably as a consequence of a peculiar mineral-mineral partitioning due to the abundant modal amount of hydrous minerals in the Finero ultramafics that falls off the one used for the calibration of these single-element geothermometers.

Table 4. Geothermobarometry.

		P (GPa)	Temperature (°C)				
Sample	**Lithology**		**Wells$_{(2px)}$**	**Ca-in opx [a]**	**Al-in ol [b]**	**Cr-in ol [b]**	**V-in ol [c]**
15-FI-30F	Ultramylonite	0.75	750	672	632	551	559
15-FI-30L	Core	0.75	695	672	645	564	601
15-FI-30G	Mylonite Core	0.75	722	668	654	569	607
15-FI-31	Protomylonite	0.75	807	684	733	652	562
15-FI-30F	Ultramylonite	-	720	-	-	-	-
15-FI-30L	Matrix	-	723	-	-	-	-
15-FI-30G	Mylonite Matrix	-	679	-	-	-	-
15-FI-24C	Harzburgite with	1.5	817	767	683	556	506
15-FI-20C	pyroxene vein	1.5	831	787	707	620	558
15-FI-23A	Dunite	1.5	829	839	709	623	618
15-FI-17		1.5	-	-	739	645	543
15-FI-21A	Ol. Websterite	1.5	-	753	731	641	620
15-FI-09	Wehrlite	1.5	-	798	791	700	641
15-FI-08B	Lherzolite	1.5	830	816	696	609	534

Calibrations: Wells $_{(2px)}$ = two-pyroxenes [43] at assumed P; [a] Nimis & Grutter, [44] at the assumed P, [b] De Hoog et al. [45]; at the assumed P; [c] Smith [46], pressure independent.

Summing up, the pervasive high-temperature deformation in the presence of a hydrous melt [16] of coarse-grained ultramafics was followed by thermal equilibration down to 750 °C. The obtained T values for mylonites s.l. are in agreement with the already published temperature estimates [1,15] indicating shearing under granulite- to upper-amphibolite facies conditions (mostly between 750 and 670 °C). These temperatures should be considered as a lower bound limit as the finer grain sizes of the mylonites will favour re-equilibration after deformation and might not record the deformation temperature.

4.2. Timing of Deformation

The Finero Complex was affected by different pre-Alpine tectonic events under granulite- to greenschist-facies conditions producing pervasive or localized foliations and isoclinal to open folds [1,15,16,28,29,32,41,47]. Discrete shear zones and pseudotachylites have received considerable attention over the past 40 years [1,15,16,29,33], but the age of the different deformation events is still debated. Altenberger [15] suggested that the shear zones were related to the Variscan cycle. Matysiak and Trepmann [33] argued that the development of mylonites was connected to extensional tectonics in Jurassic times by analogy with what was reported for other shear zones in the Ivrea-Verbano

Zone. The rare and unexpected occurrence of a single zircon grain within the fine-grained matrix of an ultramafic ultramylonitic sample (30F; Figure 10b,c) allowed us to discuss the age of activity of the shear zone. Zircon shows subround shape with lobate contours (Figure 10c). Under CL it is characterized a darker core, with a faint sector zoning, surrounded by an irregular thin rim with brighter CL emission (Figure 10c). Two LA-ICP-MS spots on this zircon provided one concordant U-Pb age at 187±3 Ma (Figure 10c) and a second discordant one (3.5% discordance) with a $^{206}Pb/^{238}U$ age of 180±4 Ma (Figure 10c and Table 5). Zircon has been observed as accessory in different lithologies within the Ph-Pd, i.e., chromitites [19,26,48] and leucocratic dykes/pods/pegmatites [26,27]. The studied zircon was possibly inherited from one of these lithologies affected by shearing.

Table 5. U-Pb zircon data.

Analyses	Isotopic Ratios						Age Estimates (Ma)						U-Pb Concordant Age (Ma)	
	$^{207}Pb/^{206}Pb$	±1σ	$^{207}Pb/^{235}U$	±1σ	$^{206}Pb/^{238}U$	±1σ	$^{207}Pb/^{206}Pb$	±1σ	$^{207}Pb/^{235}U$	±1σ	$^{206}Pb/^{238}U$	±1σ	Age	±2σ
004SMPL	0.04788	0.00056	0.18710	0.00268	0.02835	0.00036	93	1	174	2	180	2		
005SMPL	0.04987	0.00056	0.20252	0.00272	0.02946	0.00034	189	2	187	3	187	2	187.2	3.3

The obtained U-Pb data perfectly overlaps the major age peak (about 187 Ma) of zircon from chromitite layers within the mantle peridotites interpreted as the timing of exhumation at crustal levels [19]. Triassic–Jurassic U-Pb zircon ages were also reported for other mantle chromitites [48] and leucocratic dykes (225 ± 13 Ma: [27]; 190–212 Ma: [34]); they were interpreted as due to prolonged formation and multistage zircon growth in the chromitites and the timing of intrusion for the dykes, respectively. It is difficult to constrain the origin of the zircon grain analyzed in the present study based only on the U–Pb data. Nevertheless: (i) the lack of abundant chromite/spinel associated with zircon in the fine-grained matrix (Figure 10b) and (ii) the occurrence of sheared leucocratic dykes in the shear zone (Figure 2b) led us to propose that the zircon grain was likely, and luckily, inherited from the leucocratic dykes. This would suggest that the shear zone activity post-dated the Triassic-Jurassic emplacement of these dykes.

The temperature estimates combined with geochemical and microstructural observations from the sheared peridotites suggest that the Ph-Pd unit was probably still at granulite/amphibolite-facies conditions during mylonitic deformation (Figure 10a). These conditions are not compatible with deformation events that occurred during the Alpine orogenic cycle, which formed low-T shear zones at depths of about 5–10 km or less [49]. Granulite-facies conditions have been also documented for mylonites in the crustal sequence of the Finero Complex at the boundary between gabbros and peridotites [50]. Geochronological surveys suggest that these mylonites formed over a large time interval at granulite-facies conditions (ca. 230–200 Ma, [50]), with deformation likely continuing at amphibolite-facies conditions down to 180 Ma [50]. A similar age interval for deformation was proposed for the Pogallo Line (210–170 Ma, [51]), an intermediate-crust extensional shear zone interpreted in literature as the main structure accommodating necking at the Adria margin during the opening of the Alpine Tethys [52,53].

Thus, the shear zone affecting the Ph-Pd unit is one of the youngest and deepest deformation structures so far documented of a large shear system which affected the lithospheric sequence at Triassic–Jurassic times, inducing an exceptional thinning of the northernmost tip of the Ivrea-Verbano Zone and governing the exhumation of the lowermost continental crust and of the upper mantle [18,19,50,52,53].

4.3. Mineral Chemistry vs. Deformation across Shear Zone

This work reveals the occurrence of marked geochemical variations, in both major and trace element concentrations, between mylonites s.l. in a metric-scale shear zone and their coarse-grained protoliths in the Finero Ph-Pd unit. Chemical variations were also observed among rocks showing different degrees of strain within the shear zone (Figure 11). By comparing the modal composition

of the ultramylonite matrix with that of coarse-grained phlogopite harzburgites, it is observed that shearing was accompanied by a pronounced increase in the phlogopite, a significant decrease in the olivine and amphibole, and a decrease of orthopyroxene modal abundance. Clinopyroxene remains at few vol.% level. The variation in modal composition clearly indicates bulk rock chemical changes due to the interaction with percolating fluids within the shear zone. According to the field evidence, the modal composition of sheared peridotites and the ubiquitous presence of orthopyroxene and olivine porphyroclasts in ultramylonites, we concluded that the shear zone affected mainly harzburgite; therefore, we directly compare the shear zone mineral chemistry with that of coarse-grained harzburgites.

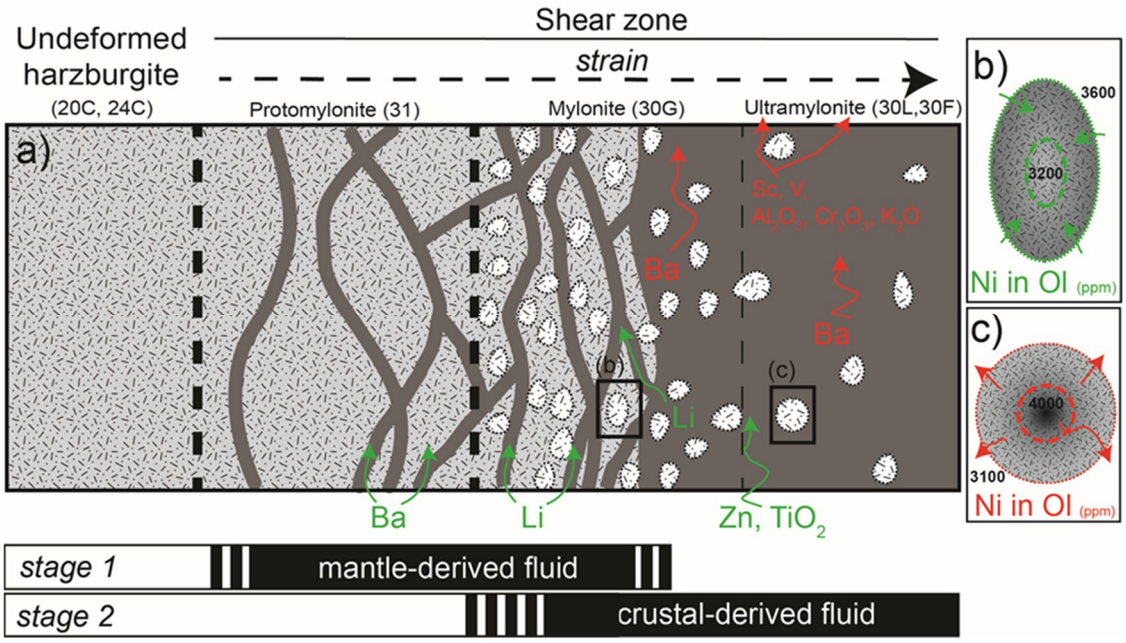

Figure 11. Cartoon summarizing the main observed variations in term of major and trace elements in the mineral phases: (**a**) Scheme of the transition from coarse-grained harzburgite to mylonite and ultramylonites. Arrows and text in red and green refer to enrichment and depletion, respectively, of elements within minerals and rocks. (**b**,**c**) Opposite chemical trends observed within olivine porphyroclasts from different sectors of the shear zone. The black bars on the bottom represent the domains of the shear zone affected by the different fluids.

4.3.1. Major Elements

In this section, the variation in major element contents of the different mineral phases from coarse-grained harzburgites to sheared peridotites is discussed, taking into account the information about the bulk rock chemistry of the studied shear zone provided [1,15]. According to these authors [1,15], the sheared peridotites experienced a gain in Al_2O_3, K_2O, and Na_2O.

Simple mass balance calculations, based on the average modal composition of coarse-grained harzburgite and the matrix composition of the ultramylonites, confirm an increase of Al_2O_3 in the bulk composition of the sheared peridotites. Considering that the Al_2O_3 content of silicates and spinel from the host coarse-grained harzburgites to the ultramylonitic domains decreases, it is suggested that the bulk gain in Al_2O_3 is the result of the profuse crystallisation (up to about 30 vol.% vs. <5 vol.% in coarse-grained harzburgites) of synkinematic phlogopite, which contains up to 14.5 wt.% Al_2O_3 (Figure S2b). The Al_2O_3 of silicates was probably also controlled by the stability of Al-bearing chromite, which is present as accessory phase within the fine-grained matrix. All these observations are consistent with the lower equilibrium T recorded by the sheared rocks (Figure 10a) promoting crystallisation hydrous minerals and chemical variation of mineral across the shear zone. In fact, it is common

wisdom that decreasing T reduces the diminishing of the substitution of Al^{3+} for Si^{4+} in tetrahedral sites of silicates (Tschermaks exchange). This decreases the capability to balance the incorporation of nondivalent elements (e.g., Al, Cr, Ti, Fe^{3+}, Mn^{3+}) in [8]-fold coordinated sites (e.g., REE^{3+} in M2 site of clinopyroxene and M4 site of amphibole; [54]), as well as the possibility of hosting Na and K in the [12]-fold coordinated sites of amphibole and phlogopite. A similar T-dependent behavior can be envisaged to explain the Cr_2O_3 content variation in mineral phases from the coarse-grained harzburgites to ultramylonites, as already proposed by Brodie [1] (Figure S2e–h).

Mass balance calculations and bulk chemistry data [1,15] also point to positive net gain of K, Na, and Ti for mylonites and ultramylonites with respect to coarse-grained harzburgites. Amphibole and phlogopite from sheared peridotites show different Na/K ratios and Na_2O and K_2O contents with respect to the coarse-grained harzburgites (Figure S2c,d). Na_2O and K_2O show opposite trends within amphibole: Na_2O increases, whereas K_2O decreases (Figure 6e,f). According to experimental investigation [55], the K/(K+Na) ratios may decrease in both amphibole and phlogopite at decreasing P and T conditions. Nevertheless, the observed variations would require changes in order of several GPa and/or hundreds of °C. Thus, it is argued that compositional variability of amphibole and phlogopite cannot be explained only by the estimated variation of P-T conditions between coarse-grained and sheared harzburgites.

Phlogopite and amphibole within the porphyroclast-poorest ultramylonite (30F) do not follow the chemical trends observed within the other sheared rocks. In particular, phlogopite is on average richer in TiO_2, K_2O and has lower Na_2O (Figure 6c and Figure S2c,d). The latter is also consistently lower in amphibole. In this sample, the geochemical variations shown by phlogopite and amphibole are accompanied by on average lower Mg# of olivine and orthopyroxene with respect to all other Ph-Pd samples. Considering that we do not observe significant differences in terms of mineral assemblages and abundances among the sheared samples, two options can be envisaged: (i) an apparent change of P-T conditions of deformation and/or (ii) a variation of the fluid percolating this sector of the shear zone.

Summing up, the major element composition of minerals in different rocks and textural positions corroborates mass transfer processes within the shear zone and fractionation effects due to the crystallization of synkinematic major phases and/or accessories. Our results based on mineral chemistry are in agreement with the results of previously published data [1,15] confirming the open system nature of the shear zone, where the mineral chemistry was partially controlled by the evolving bulk composition, fluid chemistry, and P-T conditions that modified the mineral modal proportion.

4.3.2. Minor and Trace Elements

The minor and trace elements mineral composition provide further information about the petrochemical evolution of the shear zone. The trace element concentration of the porphyroclasts from the shear zone differs significantly from the same mineral phases in the coarse-grained ultramafics, independently on their modal composition. The observed chemical differences are more likely the result of fluid–rock interaction and re-equilibration during ductile deformation than due to the heterogeneity of protoliths. The major changes are documented for Li, Co, Ni, Zn in olivine, Sc, and V in orthopyroxene, Ti, Sc, REE, and Y in clinopyroxene, and Li and Ba in phlogopite, Ba in amphibole (Figures 7 and 8). Within the shear zone, the variation in concentration of some elements is correlated to the strain intensity (i.e., porphyroclasts/matrix ratios; Figure 11b,c): Ca, Sc, and V in orthopyroxene steadily decrease on average as strain increases (Figure 7e–g), whereas Zn in olivine increases (Figure 7d). A significant drop of Sc was also observed from core to rim of orthopyroxene porphyroclasts (Figure 7f) and for amphibole (Figure 8b) from the coarse-grained harzburgites (e.g., 24C and 20C) to the protomylonites (31).

The correlation of Sc, V, and Ca content in orthopyroxene suggests that their behavior can be mainly affected by decreasing T as already argued for Al_2O_3 and Cr_2O_3. Scandium and V were likely partitioned in Al-richer silicates (clinopyroxene, amphibole, and the abundant phlogopite), whereas Cr was preferentially incorporated by spinel (Figure 5f) [56].

The progressive Zn enrichment within olivine porphyroclasts may be explained by an uptake of this element from the fluid phase by back diffusion. The availability of Zn in the fluids can be related to an external source and/or to breakdown of Zn-rich mineral phases during deformation. Olivine porphyroclasts also show a significant increase in Li, Co, and Ni from protomylonites to ultramylonites (Figure 7a–d). It is interesting to note that these elements in olivine from mantle peridotite show usually small concentration ranges being mainly partitioned by it [45].

Significant variations of Li in phlogopite and Ba in amphibole and phlogopite were observed across the shear zone even though these mineral phases are not always present as porphyroclasts in the ultramylonites (Figure 8g,h). The higher Li content of phlogopite (up to six times on average) within the high strain zone (30G) with respect to the protomylonites of the low strain zone and coarse-grained ultramafics may suggest a net in-flux of Li within the shear zone (Figure 11a). It should be noted that the highest Li contents in phlogopite and olivine were obtained from the sample of the high strain zone that represents the transition from ultramylonites to protomylonites (Figure 11a). Both phlogopite and amphibole show higher Ba contents in protomylonites with respect to those from coarse-grained protoliths and the phlogopite in the low strain zone. This highlights a net in-flux of Ba at the transition (i.e., sample 31) between the coarse-grained harzburgite and the ultramylonites.

Although clinopyroxene and amphibole porphyroclasts are not ubiquitous across the shear zone, they provide valuable insights about the geochemical evolution of the system. Amphibole composition suggests that only minor REE and HFSE changes affected the protomylonites (31); conversely, clinopyroxene porphyroclasts from mylonite (30G) and ultramylonite (30L) indicate that the high strain domain of the shear zone was significantly enriched in REE, Y, and Sr (Figure S3b). This was associated with a decrease of LREE/HREE fractionation and with an increase of REE/HFSE ratios.

Combining petrographic and microstructural features, together with the observed chemical variations, the percolation of solute-rich hydrous fluids under amphibolite/granulite facies conditions is envisaged. During such fluid–assisted shearing, porphyroclasts within the fine-grained matrix acted as both source or sink for several elements. It has been demonstrated that dislocations associated to crystal-plastic deformation are shortcuts promoting diffusion in and out of the porphyroclasts [57]. High-resolution EBSD analyses combined with further trace element mapping/profiles of the porphyroclasts are needed in order to better describe and quantify this process.

4.4. Evidence for Different Stages of Fluid–Rock Interaction

According to Altenberger [15], the shear zone experienced a long-term activity, which started under granulitic conditions, now represented by protomylonites, followed by amphibolite- to upper greenschist facies deformation event, well preserved in the ultramylonites.

Altenberger [15] demonstrated that the interaction between mylonites s.l. and fluids resulted in a modification of the whole rock chemistry by gain or loss of some elements. In the granulitic stage the shear zone suffered small volume changes, the addition of small amounts of fluids and a considerable gain of Ba, Na, Ti, and Cu, whereas other elements, such as Nb, F, and P were leached from the system [15]. Altenberger [15] also suggested that the fluid phase percolating during the granulitic stage of deformation derived probably from the upper mantle.

The trace element composition of the porphyroclasts provided in this work adds information about the origin of the fluid phase percolating during the granulitic event. The clinopyroxene porphyroclasts from the mylonitic domain of the (30G) and from ultramylonite (30L) are characterized by peculiar geochemical features. They show LREE-enriched convex-upward patterns and large REE/HFSE ratios (Figure S3b) that mimic those found in clinopyroxene from sapphirine-bearing gabbroic dykes discordantly cutting the Ph-Pd unit [17,25,41]. These magmatic products have been related to the late intrusion of mantle-derived alkali-rich melts, which promoted also metasomatic layers within the coarse-grained ultramafics. Altenberger [15] suggested a considerable whole rock gain of Ba during the granulite facies deformation. Coherently, we observe that amphibole and phlogopite from the protomylonite (31) are characterized by the highest Ba values.

An abrupt chemical change of the fluid component is documented by the low Ba values of phlogopite (<2500 ppm) from the mylonitic sector (sample 30G). These values are on average far from those reported for phlogopite within coarse-grained ultramafics, suggesting a leaching effect by the fluid. The sample (30G) represents the transition from protomylonites to ultramylonites, being composed of a mylonitic domain in contact with an ultramylonitic one. In this sample, olivine and phlogopite display the maximum values of Li. This enrichment is indicative of the presence of a recycled crustal component documented in magmatic olivine segregated from alkaline rocks, e.g., lamproites [58]. The sample (30G) is thus the transition from a sector recoding the interaction with a mantle-derived fluid (i.e., protomylonites 31) and the ultramylonitic domain of the shear zone, where a crustal-derived fluid percolated and probably erased the fingerprints of a former mantle-derived fluid.

The crustal nature of this second fluid is also supported by the chemistry of olivine porphyroclasts from ultramylonites [59,60]. Olivine from these rocks show a decoupling of Zn with respect to Ni, Co, and Li, whose partitioning is governed by olivine. This suggests a net in flux of Zn within ultramylonites, coherently with bulk rock data [15]. Zn may be carried in the form of bisulfide complexes in deep, pH neutral to basic hydrothermal systems [58]. However, Zn concentration is very low in upper mantle sulfides, whose composition is dominated by Fe and Ni, with very subordinate Cu [61]. The lack of significant deposition of synkinematic sulfides within the ultramylonites does not support the large presence of S-complexes in the second fluid, suggesting alternatively the involvement of a silicate crustal component as source of the fluid. It has been demonstrated that Zn-bearing biotite and chlorite can host large amounts of bulk Zn content in siliciclastic metasedimentary rocks [62] and altered/metasomatized mafic rocks [63], respectively. In order to explain the Zn enrichment together with the large K, Al, Ti, and Fe content recorded by the most deformed sectors of the shear zone, it is argued that dissolution of crustal biotite more likely governed the composition of the second fluid phase.

As a whole, our data confirm that the shear zone acted as a metasomatic channel, where mobility of elements was promoted by large amounts of fluids and by the increase in reaction surfaces due to deformation-induced grain size reduction, e.g., [1,15]. The results of this study highlight the role of porphyroclasts as source or sink for some elements during the fluid-assisted deformation and emphasize how they provide valuable information to unravel the nature of percolating fluids (i.e., mantle vs. crustal). It is further suggested that the trace element chemistry of porphyroclasts should be taken into account for mass balance calculation of deformed rocks. The chemical modification across shear zones is usually explained by the chemistry of synkinematic minerals and gain or loss of elements, being porphyroclasts almost neglected (at least in terms of trace elements). Here, it is demonstrated that during granulite to amphibolite facies deformation, the composition of the porphyroclasts can be severely modified by the uptake of trace and minor elements, accommodating totally or partially the changes at the bulk rock scale. In other words, the mass gain/loss in sheared rocks cannot be entirely explained by the development of synkinematic mineral assemblages.

5. Conclusions

This work provides a complete dataset on major, minor, and trace element mineral chemistry covering all the major lithologies of the Finero Phlogopite Peridotite mantle unit. These data provide valuable constraints on the relationship between geochemistry and microstructural features in ultramafic shear zones. Remarkable chemical variations are observed both for major and trace elements.

The major and trace element composition of minerals from the proto- to ultramylonites that compose the shear zone and from the coarse-grained ultramafics that are their protoliths suggest that elements were exchanged at both outcrop and crystal scale. The shear zone acted as an open system where the combined effect of fluid–rock interaction, deformation, and recrystallization resulted in marked chemical variations. The LA-ICP-MS chemical data of porphyroclasts suggest that their trace element concentrations were severely modified during deformation and that they were either source or sink for some elements. The trace element composition study of porphyroclasts was crucial to gain

information about the composition of fluid flowing through mylonites. We propose that in order to understand the chemical variations across shear zones it is fundamental to study both synkinematic minerals and porphyroclasts in terms of major and trace elements. Our study indicates that the present-day compositions of the sheared peridotites are the result of the interplay between fluids with different compositions and/or proportion with respect to the solid component and rocks showing variable microstructures.

The P-T estimates together with geochemical and microstructural observations from the studied shear zone suggest that the Ph-Pd unit was still placed at moderate depth (i.e., >15 km) under granulitic- to amphibolite facies conditions during mylonitic deformation. These conditions are not compatible with deformation events that occurred during the Alpine orogenic cycle, which formed low-T shear zones at depths of about 5–10 km or less [53]. The occurrence of a single zircon grain within the fine-grained ultramylonitic matrix allowed us to constrain the timing of deformation at 187 Ma or younger. Zircon was likely (and luckily) inherited from nearby sheared leucocratic dykes that intruded within Ph-Pd unit from the late Triassic to the early Jurassic. The results of this study confirm that the Finero Complex represents a key area for the understanding of the Mesozoic tectono-magmatic events that ruled the extension of the western margin of the Adria plate leading to the opening of the Alpine Tethys.

Supplementary Materials: The following are available online at http://www.mdpi.com/2076-3263/10/5/196/s1, Figure S1:(a) EBSD map and (b) SEM observations, Table S1: Major elements, Figure S2: Extra major elements diagrams, Table S2: Trace elements, Figure S3: PM primitive mantle-normalized trace element patterns for (a) amphibole and, (b) clinopyroxene, Table S3: Porphyroclasts profiles, Figure S4: (a) Aluminium and (b) titanium in olivine porphyroclasts profiles, Table S4: Geothermometry, Table S5: U-Pb Zircon dating.

Author Contributions: Conceptualized the study and developed methodology, A.L.; performed the formal analysis, and data curation, S.C., A.L.; prepared the original initial draft and writing, S.C., A.L. and A.Z.; supervised and provided critical reviews and editing, A.L., A.Z., A.T., and J.A.P.-N. All authors have read and agreed to the published version of the manuscript.

Funding: This research was funded by the following projects: PRIN2015 "Geochemical and isotopic budget of highly metasomatized sub-continental mantle in the Africa and Europe geodynamics systems: modern and fossil analogues"; PRIN2017 "Micro to Macro—how to unravel the nature of the large magmatic events (20178LPCPW-Langone Antonio)".

Acknowledgments: We thank the Assistant Editor Ashley Zhang and the reviewers for helpful comments that improved the manuscript. We would like to thank also the guest editors of the special issue. Part of the analyses were performed by Stefania Corvò during a short post-graduation scholarship (2018; S. Corvò) at the IGG-CNR (Pavia, Italy).

Conflicts of Interest: The authors declare no conflicts of interest.

Appendix A

Analytical methods. The major-element composition of mineral phases was determined by JEOL 8200 Electron Microprobe Analyses (EMPA) at the Dipartimento di Scienze della Terra "Ardito Desio", University of Milan. Average data and standard deviations are reported in Table 2. For mylonitic samples some maps were produced by micropobe instrument in order to study in detail the porphyroclasts and matrix composition (e.g., Figure 4). Microchemical analyses and some Back-Scattered Electron (BSE) imaging on the matrix composition were also performed by Scanning Electron Microscopy (SEM) using a Tescan Mira3 XMU-series FESEM equipped with an EDAX-EDX (accelerating voltage 20 kV, beam intensity 16.5 nA, spot area 100×100 µm, counts of 100 s., analyses and working distance 15.8 mm; University of Pavia, Italy); data was processed with EDAX Genesis software using the ZAF algorithms the correction method (Figure S1). Trace element concentrations have been determined by means of the LA-ICP-MS (laser ablation inductively coupled plasma spectrometry) at the CNR-IGG of Pavia (Italy). Average values are reported in Table 3, the whole dataset is available as Supplementary Table S2. A PerkinElmer SCIEX ELAN DCR-e quadrupole ICP-MS was coupled with a 213nm Nd:YAG laser (NewWave Research). Helium was used as carrier gas and mixed with Ar downstream of the ablation cell. Laser spot size was calibrated between 50 and 60 µm and laser

beam fluency at 8-9 J/cm^2. Data reduction was performed with GLITTER software, using the reference synthetic glass NIST (SRM) 610, NIST612 as external standards. ^{29}Si was used as internal standards for olivine, orthopyroxene, phlogopite; ^{44}Ca for clinopyroxene, and amphibole (pargasite). Precision and accuracy were assessed via repeated analyses of basalt glass (BCR-2g) reference material, resulting better than ±10% at ppm concentration level. The uncertainties related to the trace element data is of 1σ. Detection limits were typically in the range of 100-500 ppb for Sc, 10-100 ppb for Sr, Zr, Ba, Gd and Pb, 1-10 ppb for Y, Nb, La, Ce, Nd, Sm, Eu, Dy, Er, Yb. Hf and Ta, and usually <1 ppb for Pr, Th, and U. Zircon grain was analyzed in situ by laser-ablation, inductively coupled, plasma mass spectrometry (LA–ICP-MS) on 30-µm-thick sections at the CNR–Istituto di Geoscienze e Georisorse U.O. Pavia (Italy). Analytical conditions are 25 µm in diameter of spot size, 8 J/cm^2 of energy density, and 5 Hz of repetition rate. Laser-induced elemental fractionation and mass bias were corrected using zircon standard (GJ1 zircon). Data reduction was carried out with GLITTER TM software. In order to better estimate the uncertainty affecting the ^{206}Pb/^{238}U, ^{207}Pb/^{235}U isotope ratios, the external reproducibility of the standard was propagated relative to individual uncertainties for the isotope ratios. After this error propagation, each analysis is accurate within the quoted errors. The ISOPLOT 3.0 software [64] was used for age calculation. Data are reported in Table 5.

References

1. Brodie, K.H. Variations in mineral chemistry across a phlogopite shear zone. *J. Struct. Geol.* **1980**, *2*, 265–272. [CrossRef]
2. Brodie, K.H. Variation in amphibole and plagioclase composition with deformation. *Tectonophysics* **1981**, *78*, 385–402. [CrossRef]
3. Rolland, Y.; Cox, S.; Boullier, A.M.; Pennacchioni, G.; Mancktelow, N. Rare earth and trace element mobility in mid-crustal shear zones: Insights from the Mont Blanc Massif (Western Alps). *Earth Planet. Sci. Lett.* **2003**, *214*, 203–219. [CrossRef]
4. McCaig, A.M. Deep fluid circulation in fault zones. *Geology* **1988**, *16*, 867–870. [CrossRef]
5. Hidas, K.; Tommasi, A.; Garrido, C.J.; Padrón-Navarta, J.P.; Mainprice, D.; Vauchez, A.; Barou, F.; Marchesi, C. Fluid-Assisted strain localization in the shallow subcontinental lithospheric mantle. *Lithos* **2016**, *262*, 636–650. [CrossRef]
6. Précigout, J.; Prigent, C.; Palasse, L.; Pochon, A. Water pumping in mantle shear zones. *Nat. Commun.* **2017**, *8*, 15736. [CrossRef]
7. Harlov, D.E.; Austrheim, H. *Metasomatism and the Chemical Transformation of Rock—The Role of Fluids in Terrestrial and Extraterrestrial Processes*; Lecture Notes in Earth System Sciences; Spinger: Berlin, Germany, 2013; 800p.
8. Piazolo, S.; La Fontaine, A.; Trimby, P.; Harley, S.; Yang, L.; Armstrong, R.; Cairney, J.M. Deformation-Induced trace element redistribution in zircon revealed using atom probe tomography. *Nat. Commun.* **2016**, *7*, 10490. [CrossRef]
9. Kovaleva, E.; Klötzli, U.; Habler, G.; Huet, B.; Guan, Y.; Rhede, D. The effect of crystal-plastic deformation on isotope and trace element distribution in zircon: Combined BSE, CL, EBSD, FEG-EMPA and NanoSIMS study. *Chem. Geol.* **2017**, *450*, 183–198. [CrossRef]
10. O'Hara, K.; Blackburn, W. Volume-Loss model for trace element enrichments in mylonites. *Geology* **1989**, *17*, 524–527. [CrossRef]
11. Condie, K.C.; Sinha, A.K. Rare earth and other trace element mobility during mylonitization: Comparison of the Brevard and Hope Valley shear zones in the Appalachia Mountains USA. *J. Metamorph. Geol.* **1996**, *14*, 213–226. [CrossRef]
12. Tursi, F.; Festa, V.; Fornelli, A.; Micheletti, F.; Spiess, R. Syn-Shearing mobility of major elements in ductile shear zones: State of the art for felsic deformed protoliths. *Period. Mineral.* **2018**, *87*, 289–308.
13. Goncalves, P.; Oliot, E.; Marquer, D.; Connolly, J.A.D. Role of chemical processes on shear zone formation: An example from the Grimsel metagranodiorite (Aar massif, Central Alps). *J. Metamorph. Geol.* **2012**, *30*, 703–722. [CrossRef]

14. Altenberger, U. The ductile deformation of the Ivrea Zone a study from micro to mesoscale. *Mitt. Geol. Inst.* **1991**, *239*, 91–92.
15. Altenberger, U. Long-Term deformation and fluid-enhanced mass transport in a Variscan peridotite shear zone in the Ivrea Zone, northern Italy: A microtextural, petrological and geochemical study of a reactivated shear zone. *Int. J. Earth Sci.* **1995**, *84*, 591–606.
16. Tommasi, A.; Langone, A.; Padrón-Navarta, J.A.; Zanetti, A. Hydrous melts weaken the mantle, hydrous minerals do not: Insights from a petrostructural study of the Finero pargasite and phlogopite-bearing peridotites, southern Alps. *Earth Planet. Sci. Lett.* **2017**, *477*, 59–72. [CrossRef]
17. Zanetti, A.; Mazzucchelli, M.; Rivalenti, G.; Vannucci, R. The Finero phlogopite-peridotite massif: An example of subduction-related metasomatism. *Contrib. Mineral. Petrol.* **1999**, *134*, 107–122. [CrossRef]
18. Zanetti, A.; Mazzucchelli, M.; Sinigoi, S.; Giovanardi, T.; Peressini, G.; Fanning, M. SHRIMP U-Pb zircon Triassic intrusion age of the Finero mafic com-plex (Ivrea-Verbano Zone, Western Alps) and its geodynamic implications. *J. Pet.* **2013**, *54*, 2235–2265. [CrossRef]
19. Zanetti, A.; Giovanardi, T.; Langone, A.; Tiepolo, M.; Wu, F.-Y.; Dallai, L.; Mazzucchelli, M. Origin and age of zircon-bearing chromitite layers from the Finero phlogopite peridotite (Ivrea-Verbano Zone, Western Alps) and geodynamic consequences. *Lithos* **2016**, *262*, 58–74. [CrossRef]
20. Hartmann, G.; Wedepohl, K.H. The composition of peridotite tectonites from the Ivrea complex, northern Italy: Residues from melt extraction. *Geochim. Cosmochim. Acta* **1993**, *57*, 1761–1782. [CrossRef]
21. Cawthorn, R.G. The amphibole peridotite-metagabbro complex, Finero, north-ern Italy. *J. Geol.* **1975**, *83*, 437–454. [CrossRef]
22. Coltorti, M.; Siena, F. Mantle tectonite and fractionated peridotite at Finero (Italian Western Alps). *Neues Jahrb. Mineral.* **1984**, *149*, 225–244.
23. Lu, M.; Hofmann, A.W.; Mazzucchelli, M.; Rivalenti, G. The mafic-ultramafic complex near Finero (Ivrea-Verbano Zone), I: Chemistry of MORB-like magmas. *Chem. Geol.* **1997**, *140*, 207–222. [CrossRef]
24. Lu, M.; Hofmann, A.W.; Mazzucchelli, M.; Rivalenti, G. The mafic-ultramafic complex near Finero (Ivrea-Verbano Zone), I: Geochronology and isotope geochemistry. *Chem. Geol.* **1997**, *140*, 223–235. [CrossRef]
25. Giovanardi, T.; Mazzucchelli, M.; Zanetti, A.; Langone, A.; Tiepolo, M.; Cipriani, A. Occurrence of phlogopite in the Finero mafic layered complex. *Open Geosci.* **2014**, *6*, 588–613. [CrossRef]
26. Grieco, G.; Ferrario, A.; von Quadt, A.; Köppel, V.; Mathez, A. The zircon-bearing chromitites of the phlogopite peridotite of Finero (Ivrea Zone, Southern Alps): Evidence and geochronology of a metasomatized mantle slab. *J. Petrol.* **2001**, *42*, 89–101. [CrossRef]
27. Stähle, V.; Frenzel, G.; Hess, J.C.; Saupé, F.; Schmidt, S.T.; Schneider, W. Permian metabasalt and Triassic alkaline dykes in the northern Ivrea Zone: Clues to the post-Variscan geodynamic evolution of the Southern Alps. *Schweiz. Mineral. Petrogr. Mitt.* **2001**, *81*, 1–21.
28. Garuti, G.; Friolo, R. Textural features and olivine fabrics of peridotites from the Ivrea-Verbano Zone (Italian Western Alps). *Mem. Sci. Géol.* **1979**, *33*, 111–125.
29. Kruhl, J.; Voll, G. Fabrics and metamorphism from the Monte Rosa Root Zone into the Ivrea Zone near Finero, southern margin of the Alps. *Schweiz. Mineral. Petrogr. Mitt.* **1976**, *56*, 627–633.
30. Kruhl, J.; Voll, G. Deformation and metamorphism of the western Finero Com-plex. *Mem. Sci. Géol.* **1979**, *33*, 95–104.
31. Langone, A.; Padrón-Navarta, J.A.; Wei-Qiang, J.; Zanetti, A.; Mazzucchelli, M.; Tiepolo, M.; Giovanardi, T.; Bonazzi, M. Ductile-Brittle deformation effects on crystal-chemistry and U-Pb ages of magmatic and metasomatic zircons from dyke of the Finero Mafic Complex (Ivrea-Verbamo Zone, Italian Alps). *Lithos* **2017**, *284*, 493–511. [CrossRef]
32. Kenkmann, T.; Dresen, G. Dislocation microstructure and phase distribution in a lower crustal shear zone—An example from the Ivrea-Zone, Italy. *Int. J. Earth Sci.* **2002**, *91*, 445–458. [CrossRef]
33. Matysiak, A.K.; Trepmann, C.A. The deformation record of olivine in my-lonitic peridotites from the Finero Complex, Ivrea Zone: Separate deformation cycles during exhumation. *Tectonics* **2015**, *34*, 2514–2533. [CrossRef]
34. Schaltegger, U.; Ulianov, A.; Muntener, O.; Ovtcharova, M.; Peytcheva, I.; Vonlanthen, P.; Vennemann, T.W.; Antognini, M.; Girlanda, F. Megacrystic zircon with planar fractures in miaskite-type nepheline pegmatites formed at high pressures in the lower crust (Ivrea Zone, Southern Alps, Switzerland). *Am. Mineral.* **2015**, *100*, 83–94. [CrossRef]

35. Kretz, R. Symbols for rock-forming minerals. *Am. Mineral.* **1983**, *68*, 277–279.
36. Morishita, T.; Arai, S.; Green, D.H. Evolution of low-Al orthopyroxene in the Horoman Peridotite, Japan: An unusual indicator of metasomatising fluids. *J. Petrol.* **2003**, *44*, 1237–1246. [CrossRef]
37. Morishita, T.; Arai, S.; Tamura, A. Petrology of an apatite-rich layer in the Finero Phlogopite-Peridotite massif, Italian Western Alps: Implications for evolution of a metasomatizing agent. *Lithos* **2003**, *69*, 37–49. [CrossRef]
38. Morishita, T.; Hattori, K.H.; Terada, K.; Matsumoto, T.; Yamamoto, K.; Takebe, M.; Ishida, Y.; Tamura, A.; Arai, S. Geochemistry of apatite-rich layers in the Finero phlogopite-peridotite massif (ItalianWestern Alps) and ion microprobe dating of apatite. *Chem. Geol.* **2008**, *251*, 99–111. [CrossRef]
39. Ferraris, C.; Grobety, B.; Früh-Green, G.L.; Wessicken, R. Intergrowth of graphite within phlogopite from Finero ultramafic complex (Italian Western Alps): Implications for mantle crystallization of primary-texture mica. *Eur. J. Mineral.* **2004**, *16*, 899–908. [CrossRef]
40. Matsumoto, T.; Morishita, T.; Masuda, J.; Fujioka, T.; Takebe, M.; Yamamoto, K.; Arai, S. Noble gases in the Finero phlogopite-peridotites, Italian Western Alps. *Earth Planet. Sci. Lett.* **2005**, *238*, 130–145. [CrossRef]
41. Giovanardi, T.; Zanetti, A.; Dallai, L.; Morishita, T.; Hémond, C.; Mazzucchelli, M. Evidence of subduction-related components in sapphirine-bearing gabbroic dykes (Finero phlogopite-peridotite): Insights into the source of Triassic-Jurassic magmatism at the Europe-Africa boundary. *Lithos* **2020**, *356–357*, 105366. [CrossRef]
42. Lensch, G. Die ultramafitite der zone von ivrea und ihre geologische inter-pretation. *Schweiz. Mineral. Petrogr. Mitt.* **1968**, *48*, 91–102.
43. Wells, R.A. Pyroxene thermometry in simple and complex systems. *Contrib. Mineral. Petrol.* **1977**, *62*, 129–139. [CrossRef]
44. Nimis, P.; Grütter, H. Internally consistent geothermometers for garnet peridotites and pyroxenites. *Contrib. Mineral. Petrol.* **2010**, *159*, 411–427. [CrossRef]
45. De Hoog, J.C.M.; Gall, L.; Cornell, D.H. Trace-Element geochemistry of mantle olivine and application to mantle petrogenesis and geothermobarometry. *Chem. Geol.* **2010**, *270*, 196–215. [CrossRef]
46. Smith, D. Olivine thermometry and source constraints for mantle fragments in the Navajo Volcanic Field, Colorado Plateau, southwest United States: Implications for the mantle wedge. *AGU Geochem. Soc.* **2013**, *14*, 3. [CrossRef]
47. Steck, A.; Tieche, J.C. Carte geologique de l'antiforme peridotitique de Finero avec des observations sur les phases de deformation et de recristallisation. *Schweiz. Mineral. Petrogr. Mitt.* **1976**, *56*, 501–512.
48. Malitch, K.N.; Belousova, E.; Griffin, W.L.; Badanina, I.Y.; Knauf, V.V.; O'Reilly, S.Y.; Pearson, N.J. Laurite and zircon from the Finero chromitites (Italy): New insights into evolution of the subcontinental mantle. *Ore Geol. Rev.* **2019**, *90*, 210–225. [CrossRef]
49. Rutter, E.H.; Brodie, K.H.; Evans, P.J. Structural geometry, lower crustal magmatic underplating and lithospheric stretching in the Ivrea-Verbano zone, northern Italy. *J. Struct. Geol.* **1993**, *15*, 647–662. [CrossRef]
50. Langone, A.; Zanetti, A.; Daczko, N.; Piazolo, S.; Tiepolo, M.; Mazzucchelli, M. Zircon U-Pb Dating of a lower Crustal Shear zone: A case study from the Northern Sector of the Ivrea-Verbano Zone (Val Cannobina, Italy). *Tectonics* **2018**, *37*, 322–342. [CrossRef]
51. Wolff, R.; Dunkl, I.; Kiesselbach, G.; Wemmer, K.; Siegesmund, S. Ther-Mochronological constraints on the multiphase exhumation history of the Ivrea-Verbano Zone of the Southern Alps. *Tectonophysics* **2012**, *579*, 104–117. [CrossRef]
52. Decarlis, A.; Beltrando, M.; Manatschal, G.; Ferrando, S.; Carosi, R. Architecture of the Distal Piedmont-Ligurian rifted margin in NW Italy: Hints for a flip of the rift system polarity. *Tectonics* **2017**, *36*, 2388–2406. [CrossRef]
53. Petri, B.; Duretz, T.; Mohn, G.; Schmalholz, S.M.; Karner, G.D.; Muntener, O. Thinning mechanisms of heterogeneous continental lithosphere. *Earth Planet. Sci. Lett.* **2019**, *512*, 147–162. [CrossRef]
54. Tiepolo, M.; Oberti, R.; Zanetti, A.; Vannucci, R.; Foley, S.F. Trace-Element partitioning between amphibole and silicate melt. *Rev. Mineral. Geochem.* **2007**, *67*, 417–45159. [CrossRef]
55. Konzett, J.; Ulmer, P. The stability of hydrous potassic phases in lherzolitic mantle—An experimental study to 9.5 GPa in simplified and natural bulk compositions. *J. Petrol.* **2001**, *40*, 629–652. [CrossRef]

56. Witt-Eickschen, G.; O'Neill, H.S.C. The effect of temperature on the equilibrium distribution of trace elements between clinopyroxene, orthopyroxene, olivine and spinel in upper mantle peridotite. *Chem. Geol.* **2005**, *221*, 65–101. [CrossRef]
57. Chakraborty, S. Diffusion in solid silicates: A tool to track timescales of processes comes of age. *Annu. Rev. Earth Planet. Sci.* **2008**, *36*, 153–190. [CrossRef]
58. Etschmann, B.; Liu, W.; Mayanovic, R.; Mei, Y.; Heald, S.; Gordon, R.; Brugger, J. Zinc transport in hydrothermal fluids: On the roles of pressure and sulfur vs. chlorine complexing. *Am. Mineral.* **2019**, *104*, 158–161. [CrossRef]
59. Foley, S.; Prelevic, D.; Rehfeldt, T.; Jacob, D. Minor and trace elements in olivines as probes into early igneous and mantle melting processes. *Earth Planet. Sci. Lett.* **2013**, *363*, 181–191. [CrossRef]
60. Sobolev, A.V.; Hofmann, A.W.; Kuzmin, D.V.; Yaxley, G.M.; Arndt, N.T.; Chung, S.L.; Danyushevsky, L.V.; Elliott, T.; Frey, F.A.; Garcia, M.O.; et al. The amount of recycled crust in sources of mantle-derived melts. *Science* **2007**, *316*, 412–417. [CrossRef]
61. Zhang, Z.; Hirschmann, M.M. Experimental constraints on mantle sulfide melting up to 8 GPa. *Am. Mineral.* **2016**, *101*, 181–192. [CrossRef]
62. Hammerli, J.; Spandler, C.; Oliver, N.H.S.; Sossi, P.; Dipple, G.M. Zn and Pb mobility during metamorphism of sedimentary rocks and potential implications for some base metal deposits. *Miner. Depos.* **2015**, *50*, 657–664. [CrossRef]
63. White, A.J.R.; Pearce, M.A.; Meadows, H.R. Distinguishing regional-and local-scale metasomatic systems at the Prairie Downs Zn-Pb deposit. *Lithos* **2016**, *262*, 247–265. [CrossRef]
64. Ludwig, K.R. Isoplot/Ex version 3.0. A geochronological toolkit for Microsoft Excel. *Berkeley Geochron. Center* **2003**, *4*, 1–70.